

Effect of Diverse Recoding of Granule Cells on Optokinetic Response in A Cerebellar Ring Network with Synaptic Plasticity

Sang-Yoon Kim* and Woochang Lim†

*Institute for Computational Neuroscience and Department of Science Education,
Daegu National University of Education, Daegu 42411, Korea*

We consider a cerebellar ring network for the optokinetic response (OKR), and investigate the effect of diverse recoding of granule (GR) cells on OKR by varying the connection probability p_c from Golgi to GR cells. For an optimal value of p_c^* ($= 0.06$), individual GR cells exhibit diverse spiking patterns which are in-phase, anti-phase, or complex out-of-phase with respect to their population-averaged firing activity. Then, these diversely-recoded signals via parallel fibers (PFs) from GR cells are effectively depressed by the error-teaching signals via climbing fibers from the inferior olive which are also in-phase ones. Synaptic weights at in-phase PF-Purkinje cell (PC) synapses of active GR cells are strongly depressed via strong long-term depression (LTD), while those at anti- and complex out-of-phase PF-PC synapses are weakly depressed through weak LTD. This kind of “effective” depression (i.e., strong/weak LTD) at PF-PC synapses causes a big modulation in firing of PCs, which then exert effective inhibitory coordination on vestibular nucleus (VN) neuron (which evokes OKR). For the firing of VN neuron, the learning gain degree \mathcal{L}_g , corresponding to the modulation gain ratio, increases with increasing learning cycle, and it saturates at about the 300th cycle. By varying p_c from p_c^* , we find that a plot of saturated learning gain degree \mathcal{L}_g^* versus p_c forms a bell-shaped curve with a peak at p_c^* (where the diversity degree in firing of GR cells is also maximum). Consequently, the more diverse in recoding of GR cells, the more effective in motor learning for the OKR adaptation.

PACS numbers: 87.19.lw, 87.19.lu, 87.19.lv

Keywords: Optokinetic response, Effective motor learning, Diverse recoding, Granule cells, Synaptic plasticity, Cerebellar ring network

I. INTRODUCTION

The cerebellum receives information from the sensory systems, the spinal cord and other parts of the brain and then regulates motor movements. For a smoothly integrated body movement, the cerebellum activates a large set of spatially separated muscles in a precise order and timing. Thus, the cerebellum plays an essential role in fine motor control (i.e., precise spatial and temporal motor control) for coordinating voluntary movements such as posture, balance, and locomotion, resulting in smooth and balanced muscular activity [1–3]. Moreover, it is also involved in higher cognitive functions such as time perception and language processing [2, 3]. Animals and humans with damaged cerebella are still able to initiate movements, but these movements become slow, inexact, and uncoordinated [4, 5]; (a) loss of coordination of motor movement (asynergia), (b) the inability to judge distance and when to stop (dysmetria), (c) staggering walking (ataxic gait), and (d) slurred speech (ataxic dysarthria).

In the Marr-Albus-Ito theory for cerebellar computation [1, 6, 7], the cerebellum is considered to act as a simple perceptron (i.e., pattern associator) which associates input [mossy fiber (MF)] patterns with output [Purkinje cell (PC)] patterns. The input patterns become more sparse and less similar to each other via recoding process

in the granular layer. Then, the recoded inputs are fed into the PCs via the parallel fibers (PFs) [i.e., the axons of granule (GR) cells]. The PF-PC synapses are assumed to be the only synapses at which motor learning occurs. Thus, synaptic plasticity may occur at PF-PC synapses (i.e., their synaptic strengths may be potentiated or depressed). Marr in [6] assumes that a Hebbian type of long-term potentiation (LTP) (i.e., increase in synaptic strengths) occurs at the PF-PC synapses when both the pre-synaptic GR cells and the post-synaptic PCs are conjunctively excited (i.e., assumption of learning via LTP) [8, 9]. This Marr’s theory (which directly relates the cerebellar function to its structure) represents a milestone in the history of cerebellum [10]. It has also been examined in a computer simulation [11]. According to the simulation results, the overall Marr’s idea is probably right, although a few of his assumptions were wrong (e.g., binary synapses).

When the motor output is inappropriate, neurons in the inferior olive (IO) transmit error-teaching signals to the PCs through climbing fibers (CFs) (i.e., a CF signal is caused by deviation of a realized output from a desired one for the eye-movement) [12, 13]. Thus, PCs receive both the recoded PF signals (from GR cells) and the error-teaching CF signals (from IO neurons). In contrast to Marr’s learning via LTP, Albus in [7] assumes that synaptic strengths at PF-PC synapses are depressed [i.e., an anti-Hebbian type of long-term depression (LTD)] when both the PF and the CF signals are conjunctively excited. In the case of Albus’ learning via LTD, firing activities of PCs get reduced [i.e., they learn when to

*Electronic address: sykim@icn.re.kr

†Electronic address: wclim@icn.re.kr

stop their inhibition (i.e. when to disinhibit) rather than when to fire]. About 10 years later, Ito et al. in [14] have obtained clear experimental evidence for LTD; after conjunctive stimulation of the PFs and the CFs, firing activities of PCs were observed to persistently decrease. In comparison with the case of hippocampus, observation of LTD in cerebellum was so late, mainly due to small extracellular field potential denoting PF-PC transmission. This difficulty (to detect small field potentials) was overcome by employing an electronic averaging instrument, and LTD was demonstrated by directly recoding field potentials in the cerebellum [15]. Later, LTD was also observed to occur in cerebellar slices via stable recordings of extracellular field potentials [16]. Thus, LTD was established as a unique type of synaptic plasticity for cerebellar motor learning [17–19].

The spatial information of movements (e.g., amplitude or velocity) is called “gain,” while the temporal information of movements (e.g., initiation or termination) is called “timing” [20]. The goal of cerebellar motor learning is to perform precise gain and temporal control for movements. The cerebellar mechanisms for gain and timing control for eye movements have been studied in the two types of experimental paradigms; (1) gain control for the optokinetic response (OKR) and the vestibulo-ocular reflex [1, 21] and (2) timing control for the eyeblink conditioning [22, 23]. Here, we are concerned about gain adaptation of OKR. When the eye tracks a moving object with the stationary head, OKR may be seen. When the moving object is out of the field of vision, the eye moves back rapidly to the original position where it first saw. In this way, OKR consists of two consecutive slow and fast phases.

Experimental works on OKR in vertebrates such as rabbits, mice, and zebrafishes have been done in diverse aspects [24–31]. In addition, computational works on OKR have also been performed [20, 32]. The Marr-Albus model of the cerebellum was also reformulated to incorporate dynamical responses in terms of the adaptive filter model (used in the field of engineering control) [33, 34]. The cerebellar structure may be mapped onto an adaptive filter structure. Through analysis-synthesis process of the adaptive filter model, the (time-varying) filter inputs (i.e., MF “context” signals for the post-eye-movement) are analyzed into diverse component signals (i.e., diversely recoded PF signals). Then, they are weighted (i.e., synaptic plasticity at PF-PC synapse) and recombined to generate the filter output (i.e., firing activity of PCs). The filter is adaptive because its weights are adjusted by an error-teaching signal (i.e., CF signal), employing the covariance learning rule [35]. Using this adaptive filter model, gain adaptation of OKR was successfully simulated [32]. Recently, Yamazaki and Nagao in [20] employed a spiking network model, which was originally introduced for Pavlovian delay eyeblink conditioning [36]. As elements in the spiking network, leaky integrate-and-fire neuron models were used, and parameter values for single cells and synaptic currents were

adopted from physiological data. Through a large-scale computer simulation, some features of OKR adaptation were successfully reproduced.

However, the effects of diverse recoding of GR cells on OKR adaption in previous computational works are still needed to be more clarified in several dynamical aspects. First of all, dynamical classification of diverse PF signals (corresponding to the recoded outputs of GR cells) must be completely done for clear understanding their association with the error-teaching CF signals. Then, based on such dynamical classification of diverse spiking patterns of GR cells, synaptic plasticity at PF-PC synapses and the subsequent learning progress could be more clearly understood. As a result, understanding on the learning gain and the learning progress for the OKR adaptation is expected to be so much improved.

To this end, we consider a cerebellar spiking ring network for the OKR adaptation, and first make a dynamical classification of diverse spiking patterns of GR cells (i.e., diverse PF signals) by changing the connection probability p_c from Golgi (GO) to GR cells in the granular layer. An instantaneous whole-population spike rate $R_{GR}(t)$ (which is obtained from the raster plot of spikes of individual neurons) may well describe collective firing activity in the whole population of GR cells [37–44]. $R_{GR}(t)$ is in-phase with respect to the sinusoidally-modulating MF input signal for the post-eye-movement, although it has a central flattened plateau due to inhibitory inputs from GO cells.

The whole population of GR cells is divided into GR clusters. These GR clusters show diverse spiking patterns which are in-, anti-, and complex out-of-phase relative to the instantaneous whole-population spike rate $R_{GR}(t)$. Each spiking pattern is characterized in terms of the “conjunction” index, denoting the resemblance (or similarity) degree between the spiking pattern and the instantaneous whole-population spike rate $R_{GR}(t)$. To quantify the degree of diverse recording of GR cells, we introduce the diversity degree \mathcal{D} , given by the relative standard deviation in the distribution of conjunction indices of all spiking patterns. We mainly consider an optimal case of $p_c^*(= 0.06)$ where the spiking patterns of GR clusters are the most diverse. In this case, $\mathcal{D}^* \simeq 1.613$ which is a quantitative measure for diverse recoding of GR cells in the granular layer.

Next, based on dynamical classification of diverse spiking patterns of GR clusters, we employ a refined rule for synaptic plasticity (constructed from the experimental result in [12]) and make an intensive investigation on the effect of diverse recoding of GR cells on synaptic plasticity at PF-PC synapses and subsequent learning process. PCs (corresponding to the cerebellar output) receive both the diversely-recoded PF signals from GR cells and the error-teaching CF signals from the IO neuron. We also note that the CF signals are in-phase with respect to the instantaneous whole-population spike rate $R_{GR}(t)$. In this case, CF signals may be regarded as “instructors,” while PF signals can be considered as “stu-

dents.” Then, in-phase PF student signals are strongly depressed (i.e., their synaptic weights at PF-PC synapse are greatly decreased) by the in-phase CF instructor signals.

On the other hand, out-of-phase PF student signals are weakly depressed (i.e., their synaptic weights at PF-PC synapses are a little decreased) due to the phase difference between the student PF and the instructor CF signals. In this way, at the PF-PC synapses, the PF student signals are effectively depressed by the error-teaching CF instructor signals. This kind of effective depression at PF-PC synapses may cause a big modulation in firing activities of PCs, which then exert effective inhibitory coordination on vestibular nucleus (VN) neuron (which evokes OKR eye-movement). For the firing activity of VN neuron, the learning gain degree \mathcal{L}_g , corresponding to the modulation gain ratio (i.e., normalized modulation divided by that at the 1st cycle), increases with learning cycle, and it eventually becomes saturated.

Saturation in learning progress is clearly shown in the IO system. During the learning cycle, the IO neuron receives both the excitatory sensory signal for a desired eye-movement and the inhibitory signal from the VN neuron (representing a realized eye-movement). We introduce the learning progress degree \mathcal{L}_p , given by the ratio of the time-averaged inhibitory input from the VN neuron to the time-averaged excitatory input of the desired sensory signal. With increasing cycle, the time-averaged inhibition (from the VN neuron) increases (i.e., \mathcal{L}_p increases), and converges to the constant time-averaged excitation (from the desired signal). Thus, at about the 300th cycle, the learning progress degree becomes saturated at $\mathcal{L}_p = 1$. At this saturated stage, the time-averaged excitatory and inhibitory inputs to the IO neuron become balanced, and we get the saturated learning gain degree $\mathcal{L}_g^* (\simeq 1.608)$ in the VN.

By changing p_c from p_c^* ($= 0.06$), we also investigate the effect of diverse recoding of GR cells on the OKR adaptation. Thus, the plot of saturated learning gain degree \mathcal{L}_g^* versus p_c is found to form a bell-shaped curve with a peak at p_c^* . With increasing or decreasing p_c from p_c^* , the diversity degree \mathcal{D} in firing activities of GR cells also has its maximum value $\mathcal{D}^* \simeq 1.613$ at p_c^* . Thus, both the saturated learning gain degree \mathcal{L}_g^* and the diversity degree \mathcal{D} have a strong correlation with the Pearson’s correlation coefficient $r \simeq 0.9998$ [45]. Consequently, the more diverse in recoding of GR cells, the more effective in motor learning for the OKR adaptation.

This paper is organized as follows. In Sec. II, we describe the cerebellar ring network for the OKR, composed of the granular layer, the Purkinje-molecular layer, and the VN-IO part. The governing equations for the population dynamics in the ring network are also presented, along with a refined rule for the synaptic plasticity at the PF-PC synapses. Then, in the main Sec. III, we investigate the effect of diverse recoding of GR cells on motor learning for the OKR adaptation by changing p_c . Finally, we give summary and discussion in Sec. IV.

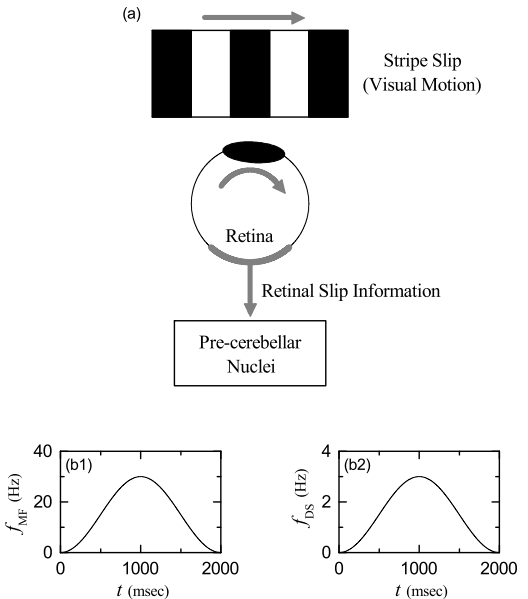


FIG. 1: (a) Optokinetic response when the eye tracks stripe slip. External sensory signals: (b1) firing rate $f_{MF}(t)$ of the mossy-fiber (MF) context signal for the post-eye-movement and (b2) firing rate $f_{DS}(t)$ of the inferior olive (IO) desired signal for a desired eye-movement.

II. CEREBELLAR RING NETWORK WITH SYNAPTIC PLASTICITY

In this section, we describe our cerebellar ring network with synaptic plasticity for the OKR adaptation. Figure 1(a) shows OKR which may be seen when the eye tracks successive stripe slip with the stationary head. When each moving stripe is out of the field of vision, the eye moves back quickly to the original position where it first saw. Thus, OKR is composed of two consecutive slow and fast phases (i.e., slow tracking eye-movement and fast reset saccade). It takes 2 sec (corresponding to 0.5 Hz) for one complete slip of each stripe. Slip of the visual image across large portions of the retina is the stimulus that stimulates optokinetic eye movements, and also the stimulus that produces the adaptation of the optokinetic system.

A. MF Context Signal and IO Desired Signal

There are two types of sensory signals which transfer the retinal slip information from the retina to their targets by passing intermediate pre-cerebellar nuclei (PCN). In the 1st case, the retinal slip information first passes the pretectum in the midbrain, then passes the nucleus reticularis tegmentis pontis (N RTP) in the pons, and finally it is transferred to the granular layer (consisting of GR and GO cells) in the cerebellar cortex via MF sensory signal containing “context” for the post-eye-movement.

The MF context signals are modeled in terms of Poisson spike trains which modulate sinusoidally at the stripe-slip frequency $f_s = 0.5$ Hz (i.e., one-cycle period: 2 sec) with the peak firing rate of 30 Hz (i.e., 30 spikes/sec) [20]. The firing frequency f_{MF} of Poisson spike trains for the MF context signal is given by

$$f_{MF} = -\bar{f}_{MF} \cos(2\pi f_s t) + \bar{f}_{MF}; \quad \bar{f}_{MF} = 15 \text{ Hz}, \quad (1)$$

which is shown in Fig. 1(b1).

In the 2nd case, the retinal slip information passes only the pretectum, and then (without passing NRTP) it is directly fed into to the IO via a sensory signal for a “desired” eye-movement. As in the MF context signals, the IO desired signals are also modeled in terms of the same kind of sinusoidally modulating Poisson spike trains at the stripe-slip frequency $f_s = 0.5$ Hz. The firing frequency f_{DS} of Poisson spike trains for the IO desired signal (DS) is given by:

$$f_{DS} = -\bar{f}_{DS} \cos(2\pi f_s t) + \bar{f}_{DS}; \quad \bar{f}_{DS} = 1.5 \text{ Hz}, \quad (2)$$

which is shown in Fig. 1(b2). In this case, the peak firing rate for the IO desired signal is reduced to 3 Hz to satisfy low mean firing rates (~ 1.5 Hz) of individual IO neurons (i.e., corresponding to 1/10 of the peak firing rate of the MF signal) [46, 47].

B. Architecture for Cerebellar Ring Network

The box diagram for the cerebellar network and our cerebellar ring network for the OKR are shown in Fig. 2. In Fig. 2(a), the granular layer, corresponding to the input layer of the cerebellar cortex, consists of the excitatory GR cells and the inhibitory GO cells. On the other hand, the Purkinje-molecular layer, corresponding to the output layer of the cerebellar cortex, is composed of the inhibitory PCs and the inhibitory BCs (basket cells). The MF context signal for the post-eye-movement is fed from the PCN (pre-cerebellar nuclei) to the GR cells. They are diversely recorded via inhibitory coordination of GO cells on GR cells in the granular layer. Then, these diversely-recoded outputs are fed via PFs to the PCs and the BCs in the Purkinje-molecular layer.

The PCs receive another excitatory error-teaching CF signals from the IO, along with the inhibitory inputs from BCs. Then, depending on the type of PF signals (i.e., in- or out-of-phase PF signals), diverse PF (student) signals are effectively depressed by the (in-phase) error-teaching (instructor) CF signals. Such effective depression at PF-PC synapses causes a large modulation in firing activities of PCs (principal output cells in the cerebellar cortex). Then, the VN neuron generates the final output of the cerebellum (i.e., it evokes OKR eye-movement) through receiving both the inhibitory inputs from the PCs and the excitatory inputs via MFs. This VN neuron also provides inhibitory inputs for the realized eye-movement to the IO neuron which also receives the excitatory desired signals

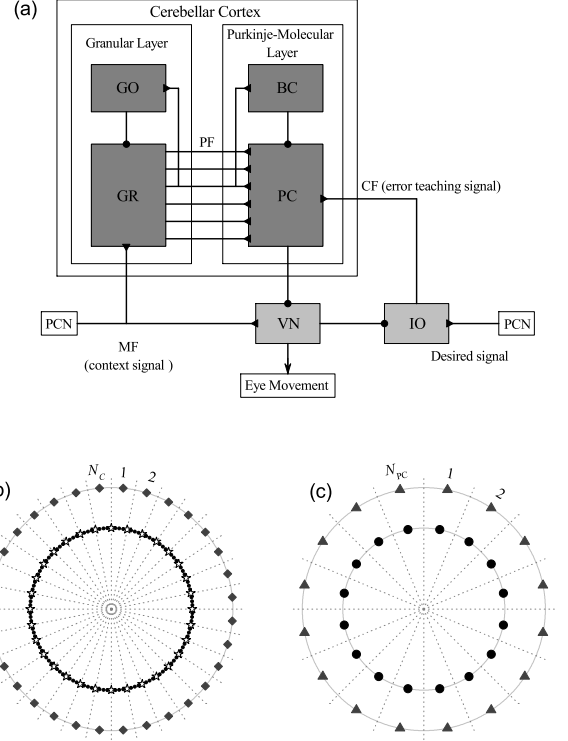


FIG. 2: Cerebellar Ring Network. (a) Box diagram for the cerebellar network. Lines with triangles and circles denote excitatory and inhibitory synapses, respectively. GR (granule cell), GO (Golgi cell), and PF (parallel fiber) in the granular layer, PC (Purkinje cell) and BC (basket cell) in the Purkinje-molecular layer, and other parts for VN (vestibular nuclei), IO(inferior olive), PCN(pre-cerebellar nuclei), MF (mossy fiber), and CF (climbing fiber). (b) Schematic diagram for granular-layer ring network with concentric inner GR and outer GO rings. Numbers represent granular layer zones (bounded by dotted lines) for $N_C = 32$. In each I th zone ($I = 1, \dots, N_C$), there exists the I th GR cluster on the inner GR ring. Each GR cluster consists of GR cells (solid circles), and it is bounded by 2 glomeruli (stars). On the outer GO ring in the I th zone, there exists the I th GO cell (diamonds). (c) Schematic diagram for Purkinje-molecular-layer ring network with concentric inner PC and outer BC rings. Numbers represent the Purkinje-molecular-layer zones (bounded by dotted lines) for $N_{PC} = 16$. In each J th zone, there exist the J th PC (solid circle) on the inner PC ring and the J th BC (solid triangle) on the outer BC ring.

for a desired eye-movement from the PCN. Then, the IO neuron supplies excitatory error-teaching CF signals to the PCs.

Figure 2(b) shows a schematic diagram for the granular-layer ring network with concentric inner GR and outer GO rings. Numbers represent granular-layer zones (bounded by dotted lines). That is, the numbers 1, 2, ..., and N_C denote the 1st, the 2nd, ..., and the N_C th granular-layer zones, respectively. Hence, the total number of granular-layer zones is N_C ; Fig. 2(b)

shows an example for $N_C = 32$. In each I th zone ($I = 1, \dots, N_C$), there exists the I th GR cluster on the inner GR ring. Each GR cluster consists of N_{GR} excitatory GR cells (solid circles). Then, location of each GR cell may be represented by the two indices (I, i) which represent the i th GR cell in the I th GR cluster, where $i = 1, \dots, N_{GR}$. Here, we consider the case of $N_C = 2^{10}$ and $N_{GR} = 50$, and hence the total number of GR cells is 51,200. In this case, the I th zone covers the angular range of $(I-1) \theta_{GR}^* < \theta < I \theta_{GR}^*$ ($\theta_{GR}^* = 0.35^\circ$). On the outer GO ring in each I th zone, there exists the I th inhibitory GO cell (diamond), and hence the total number of GO cells is N_C .

We note that each GR cluster is bounded by 2 glomeruli (corresponding to the axon terminals of the MFs) (stars). GR cells within each GR cluster share the same inhibitory and excitatory synaptic inputs through their dendrites which contact the two glomeruli at both ends of the GR cluster. Each glomerulus receives inhibitory inputs from nearby 81 (clockwise side: 41 and counter-clockwise side: 40) GO cells with a random connection probability p_c ($= 0.06$). Hence, on average, about 5 GO cell axons innervate each glomerulus. Thus, each GR cell receives about 10 inhibitory inputs through 2 dendrites which synaptically contact the glomeruli at both boundaries. In this way, each GR cell in the GR cluster shares the same inhibitory synaptic inputs from nearby GO cells through the intermediate glomeruli at both ends.

Also, each GR cell shares the same two excitatory inputs via the two glomeruli at both boundaries, because a glomerulus receives an excitatory MF input. Here, we take into consideration stochastic variability of synaptic transmission from a glomerulus to GR cells, and supply independent Poisson spike trains with the same firing rate to each GR cell for the excitatory MF signals. In this GR-GO feedback system, each GO cell receives excitatory synaptic inputs via PFs from GR cells in the nearby 49 (central side: 1, clockwise side: 24 and counter-clockwise side: 24) GR clusters with a random connection probability 0.1. Thus, 245 PFs (i.e. GR cell axons) innervate a GO cell.

Figure 2(c) shows a schematic diagram for the Purkinje-molecular-layer ring network with concentric inner PC and outer BC rings. Numbers denote the Purkinje-molecular-layer zones (bounded by dotted lines). In each J th zone ($J = 1, \dots, N_{PC}$), there exist the J th PC (solid circles) on the inner PC ring and the J th BC (solid triangles) on the outer BC ring. Here, we consider the case of $N_{PC} = 16$, and hence the total numbers of PC and BC are 16, respectively. In this case, each J th ($J = 1, \dots, N_{PC}$) zone covers the angular range of $(J-1) \theta_{PC}^* < \theta < J \theta_{PC}^*$, where $\theta_{PC}^* \simeq 22.5^\circ$ (corresponding to about 64 zones in the granular-layer ring network). We note that diversely-recoded PFs innervate PCs and BCs. Each PC (BC) in the J th Purkinje-molecular-layer zone receives excitatory synaptic inputs via PFs from all the GR cells in the 288 GR clusters (clockwise side: 144

and counter-clockwise side: 144 when starting from the angle $\theta = (J-1) \theta_{PC}^*$ in the granular-layer ring network). Thus, each PC (BC) is synaptically connected via PFs to the 14,400 GR cells (which corresponds to about 28 % of the total GR cells). In addition to the PF signals, each PC also receives inhibitory inputs from nearby 3 BCs (central side: 1, clockwise side: 1 and counter-clockwise side: 1) and excitatory error-teaching CF signal from the IO.

Outside the cerebellar cortex, for simplicity, we consider just one VN neuron and one IO neuron. Both excitatory inputs from 100 MFs and inhibitory inputs from all the 16 PCs are fed into the VN neuron. Then, the VN neuron evokes the OKR eye-movement and supplies inhibitory input for the realized eye-movement to the IO neuron. One additional excitatory desired signal from the PCN is also fed into the IO neuron. Then, through integration of both excitatory and inhibitory inputs, the IO neuron provides excitatory error-teaching CF signals to the PCs.

C. Leaky Integrate-And-Fire Neuron Model with Afterhyperpolarization Current

As elements of the cerebellar ring network, we choose leaky integrate-and-fire (LIF) neuron models which incorporate additional afterhyperpolarization (AHP) currents that determine refractory periods [48]. This LIF neuron model is one of the simplest spiking neuron models. Due to its simplicity, it can be easily analyzed and simulated. Thus, it has been very popularly used as a neuron model.

The following equations govern dynamics of states of individual neurons in the X population:

$$C_X \frac{dv_i^{(X)}}{dt} = -I_{L,i}^{(X)} - I_{AHP,i}^{(X)} + I_{ext}^{(X)} - I_{syn,i}^{(X)}, \quad i = 1, \dots, N_X, \quad (3)$$

where N_X is the total number of neurons in the X population, $X = \text{GR}$ and GO in the granular layer, $X = \text{PC}$ and BC in the Purkinje-molecular layer, and in the other parts $X = \text{VN}$ and IO . In Eq. (1), C_X (pF) represents the membrane capacitance of the cells in the X population, and the state of the i th neuron in the X population at a time t (msec) is characterized by its membrane potential $v_i^{(X)}$ (mV). The time-evolution of $v_i^{(X)}(t)$ is governed by 4 types of currents (pA) into the i th neuron in the X population; the leakage current $I_{L,i}^{(X)}$, the AHP current $I_{AHP,i}^{(X)}$, the external constant current $I_{ext}^{(X)}$ (independent of i), and the synaptic current $I_{syn,i}^{(X)}$.

We note that the equation for a single LIF neuron model [without the AHP current and the synaptic current in Eq. (3)] describes a simple parallel resistor-capacitance (RC) circuit. Here, the leakage term is due to the resistor and the integration of the external current is due to the capacitor which is in parallel to the resistor. Thus, in

Eq. (3), the 1st type of leakage current $I_{L,i}^{(X)}$ for the i th neuron in the X population is given by:

$$I_{L,i}^{(X)} = g_L^{(X)}(v_i^{(X)} - V_L^{(X)}), \quad (4)$$

where $g_L^{(X)}$ and $V_L^{(X)}$ are conductance (nS) and reversal potential for the leakage current.

When the membrane potential $v_i^{(X)}$ reaches a threshold $v_{th}^{(X)}$ at a time $t_{f,i}^{(X)}$, the i th neuron fires a spike. After firing (i.e., $t \geq t_{f,i}^{(X)}$), the 2nd type of AHP current $I_{AHP,i}^{(X)}$ follows:

$$I_{AHP,i}^{(X)} = g_{AHP}^{(X)}(t) (v_i^{(X)} - V_{AHP}^{(X)}) \quad \text{for } t \geq t_{f,i}^{(X)}. \quad (5)$$

Here, $V_{AHP}^{(X)}$ is the reversal potential for the AHP current, and the conductance $g_{AHP}^{(X)}(t)$ is given by an exponential-decay function:

$$g_{AHP}^{(X)}(t) = \bar{g}_{AHP}^{(X)} e^{-(t-t_{f,i}^{(X)})/\tau_{AHP}^{(X)}}, \quad (6)$$

where $\bar{g}_{AHP}^{(X)}$ and $\tau_{AHP}^{(X)}$ are the maximum conductance and the decay time constant for the AHP current. As $\tau_{AHP}^{(X)}$ increases, the refractory period becomes longer.

The 3rd type of external constant current $I_{ext}^{(X)}$ for the cellular spontaneous discharge is supplied to only PCs and VN neuron because of their high spontaneous firing rates [49, 50]. In Appendix, Table I shows the parameter values for the capacitance C_X , the leakage current $I_L^{(X)}$, the AHP current $I_{AHP}^{(X)}$, and the external constant current $I_{ext}^{(X)}$. These values are adopted from physiological data [20, 36].

D. Synaptic Currents

The 4th type of synaptic current $I_{syn,i}^{(X)}$ into the i th neuron in the X population consists of the following 3 kinds of synaptic currents:

$$I_{syn,i}^{(X)} = I_{AMPA,i}^{(X,Y)} + I_{NMDA,i}^{(X,Y)} + I_{GABA,i}^{(X,Z)}. \quad (7)$$

Here, $I_{AMPA,i}^{(X,Y)}$ and $I_{NMDA,i}^{(X,Y)}$ are the excitatory AMPA (α -amino-3-hydroxy-5-methyl-4-isoxazolepropionic acid) receptor-mediated and NMDA (N -methyl- D -aspartate) receptor-mediated currents from the pre-synaptic source Y population to the post-synaptic i th neuron in the target X population. On the other hand, $I_{GABA,i}^{(X,Z)}$ is the inhibitory GABA_A (γ -aminobutyric acid type A) receptor-mediated current from the pre-synaptic source Z population to the post-synaptic i th neuron in the target X population.

Similar to the case of the AHP current, the R (= AMPA, NMDA, or GABA) receptor-mediated synaptic current $I_{R,i}^{(T,S)}$ from the pre-synaptic source S population

to the i th post-synaptic neuron in the target T population is given by:

$$I_{R,i}^{(T,S)} = g_{R,i}^{(T,S)}(t) (v_i^{(T)} - V_R^{(S)}), \quad (8)$$

where $g_{R,i}^{(T,S)}(t)$ and $V_R^{(S)}$ are synaptic conductance and synaptic reversal potential (determined by the type of the pre-synaptic source S population), respectively. We get the synaptic conductance $g_{R,i}^{(T,S)}(t)$ from:

$$g_{R,i}^{(T,S)}(t) = \bar{g}_R^{(T)} \sum_{j=1}^{N_S} J_{ij}^{(T,S)} w_{ij}^{(T,S)} s_j^{(T,S)}(t), \quad (9)$$

where $\bar{g}_R^{(T)}$ and $J_{ij}^{(T,S)}$ are the maximum conductance and the synaptic weight of the synapse from the j th pre-synaptic neuron in the source S population to the i th post-synaptic neuron in the target T population, respectively. The inter-population synaptic connection from the source S population to the target T population is given by the connection weight matrix $W^{(T,S)}$ ($= \{w_{ij}^{(T,S)}\}$) where $w_{ij}^{(T,S)} = 1$ if the j th neuron in the source S population is pre-synaptic to the i th neuron in the target T population; otherwise $w_{ij}^{(T,S)} = 0$.

The post-synaptic ion channels are opened due to the binding of neurotransmitters (emitted from the source S population) to receptors in the target T population. The fraction of open ion channels at time t is represented by $s_j^{(T,S)}(t)$. The time course of $s_j^{(T,S)}(t)$ of the j th neuron in the source S population is given by a sum of exponential-decay functions $E_R^{(T,S)}(t - t_f^{(j)})$:

$$s_j^{(T,S)}(t) = \sum_{f=1}^{F_j^{(S)}} E_R^{(T,S)}(t - t_f^{(j)}), \quad (10)$$

where $t_f^{(j)}$ and $F_j^{(S)}$ are the f th spike time and the total number of spikes of the j th neuron in the source S population, respectively. The exponential-decay function $E_R^{(T,S)}(t)$ (which corresponds to contribution of a pre-synaptic spike occurring at $t = 0$ in the absence of synaptic delay) is given by:

$$E_R^{(T,S)}(t) = e^{-t/\tau_R^{(T)}} \Theta(t) \quad \text{or} \quad (11a)$$

$$= (A_1 e^{-t/\tau_{R,1}^{(T)}} + A_2 e^{-t/\tau_{R,2}^{(T)}}) \Theta(t), \quad (11b)$$

where $\Theta(t)$ is the Heaviside step function: $\Theta(t) = 1$ for $t \geq 0$ and 0 for $t < 0$. Depending on the source and the target populations, $E_R^{(T,S)}(t)$ may be a type-1 single exponential-decay function of Eq. (11a) or a type-2 dual exponential-decay function of Eq. (11b). In the type-1 case, there exists one synaptic decay time constant $\tau_R^{(T)}$ (determined by the receptor on the post-synaptic target T population), while in the type-2 case, two synaptic decay time constants, $\tau_{R,1}^{(T)}$ and $\tau_{R,2}^{(T)}$ exist. In most cases, the type-1 single exponential-decay function of Eq. (11a)

appears, except for the two synaptic currents $I_{\text{GABA}}^{(\text{GR},\text{GO})}$ and $I_{\text{NMDA}}^{(\text{GO},\text{GR})}$.

In Appendix, Table II shows the parameter values for the maximum conductance $\bar{g}_R^{(T)}$, the synaptic weight $J_{ij}^{(T,S)}$, the synaptic reversal potential $V_R^{(S)}$, the synaptic decay time constant $\tau_R^{(T)}$, and the amplitudes A_1 and A_2 for the type-2 exponential-decay function in the granular layer, the Purkinje-molecular layer, and the other parts for the VN and IO, respectively. These values are adopted from physiological data [20, 36].

E. Synaptic Plasticity

In this work, we employ a refined rule for synaptic plasticity, based on the experimental result in [12]. The coupling strength of the synapse from the pre-synaptic

neuron j in the source S population to the post-synaptic neuron i in the target T population is $J_{ij}^{(T,S)}$. Initial synaptic strengths are given in Table II. Here, we assume that learning occurs only at the PF-PC synapses. Hence, only the synaptic strengths $J_{ij}^{(\text{PC},\text{PF})}$ of PF-PC synapses may be modifiable, while synaptic strengths of all the other synapses are static. [Here, the index j for the PFs corresponds to the two indices (M, m) for GR cells representing the m th ($1 \leq m \leq 50$) cell in the M th ($1 \leq M \leq 2^{10}$) GR cluster.] Synaptic plasticity at PF-PC synapses have been so much studied in diverse experimental [12, 14–17, 51–59] and computational [7, 11, 20, 36, 60–66] works.

With increasing time t , synaptic strength for each PF-PC synapse is updated with the following multiplicative rule (depending on states) [12]:

$$J_{ij}^{(\text{PC},\text{PF})}(t) \rightarrow J_{ij}^{(\text{PC},\text{PF})}(t) + \Delta\text{LTD}^{(1)} + \Delta\text{LTD}^{(2)} + \Delta\text{LTP}, \quad (12)$$

where

$$\Delta\text{LTD}^{(1)} = -\delta_{\text{LTD}} \cdot J_{ij}^{(\text{PC},\text{PF})}(t) \cdot CF_i(t) \cdot \sum_{\Delta t=0}^{\Delta t_r^*} \Delta J_{\text{LTD}}(\Delta t), \quad (13)$$

$$\Delta\text{LTD}^{(2)} = -\delta_{\text{LTD}} \cdot J_{ij}^{(\text{PC},\text{PF})}(t) \cdot [1 - CF_i(t)] \cdot PF_{ij}(t) \cdot D_i(t) \cdot \sum_{\Delta t=0}^{\Delta t_l^*} \Delta J_{\text{LTD}}(\Delta t), \quad (14)$$

$$\Delta\text{LTP} = \delta_{\text{LTP}} \cdot [J_0^{(\text{PC},\text{PF})} - J_{ij}^{(\text{PC},\text{PF})}(t)] \cdot [1 - CF_i(t)] \cdot PF_{ij}(t) \cdot [1 - D_i(t)]. \quad (15)$$

Here, $J_0^{(\text{PC},\text{PF})}$ is the initial value ($=0.006$) for the synaptic strength of PF-PC synapses. Synaptic modification (LTD or LTP) occurs, depending on the relative time difference Δt [$= t_{\text{CF}} (\text{CF activation time}) - t_{\text{PF}} (\text{PF activation time})$] between the spiking times of the error-teaching instructor CF and the diversely-recoded student PFs. In Eqs. (13)–(15), $CF_i(t)$ represents a spike train of the CF signal coming into the i th PC. When $CF_i(t)$ activates at a time t , $CF_i(t) = 1$; otherwise, $CF_i(t) = 0$. This instructor CF firing causes LTD at PF-PC synapses in conjunction with earlier ($\Delta t > 0$) student PF firings in the range of $t_{\text{CF}} - \Delta t_r^* < t_{\text{PF}} < t_{\text{CF}}$ ($\Delta t_r^* \simeq 277.5$ msec), which corresponds to the major LTD in Eq. (13).

We next consider the case of $CF_i(t) = 0$, corresponding to Eqs. (14) and (15). Here, $PF_{ij}(t)$ denotes a spike train of the PF signal from the j th pre-synaptic GR cell to the i th post-synaptic PC. When $PF_{ij}(t)$ activates at time t , $PF_{ij}(t) = 1$; otherwise, $PF_{ij}(t) = 0$. In the case of $PF_{ij}(t) = 1$, PF firing may give rise to LTD or LTP, depending on the presence of earlier CF firings in an effective range. If CF firings exist in the range of $t_{\text{PF}} + \Delta t_l^* < t_{\text{CF}} < t_{\text{PF}}$ ($\Delta t_l^* \simeq -117.5$ msec), $D_i(t) =$

1; otherwise $D_i(t) = 0$. When both $PF_{ij}(t) = 1$ and $D_i(t) = 1$, the PF firing causes another LTD at PF-PC synapses in association with earlier ($\Delta t < 0$) CF firings [see Eq. (14)]. The likelihood for occurrence of earlier CF firings within the effective range is very low because mean firing rates of the CF signals (corresponding to output firings of individual IO neurons) are ~ 1.5 Hz [46, 47]. Hence, this 2nd type of LTD is a minor one. On the other hand, in the case of $D_i(t) = 0$ (i.e., absence of earlier associated CF firings), LTP occurs due to the PF firing alone [see Eq. (15)]. The update rate δ_{LTD} for LTD in Eqs. (13) and (14) is 0.005, while the update rate δ_{LTP} for LTP in Eqs. (15) is 0.0005 ($=\delta_{\text{LTD}}/10$).

In the case of LTD in Eqs. (13) and (14), the synaptic modification $\Delta J_{\text{LTD}}(\Delta t)$ varies depending on the relative time difference Δt ($= t_{\text{CF}} - t_{\text{PF}}$). We employ the following time window for the synaptic modification $\Delta J_{\text{LTD}}(\Delta t)$ [12]:

$$\Delta J_{\text{LTD}}(\Delta t) = A + B \cdot e^{-(\Delta t - t_0)^2/\sigma^2}, \quad (16)$$

where $A = -0.12$, $B = 0.4$, $t_0 = 80$, and $\sigma = 180$. Figure 3 shows the time window for $\Delta J_{\text{LTD}}(\Delta t)$. As shown well

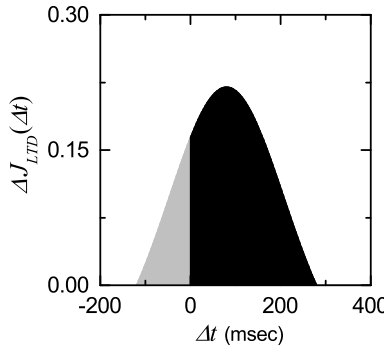


FIG. 3: Time window for the LTD at the PF-PC synapse. Plot of synaptic modification $\Delta J_{LTD}(\Delta t)$ for LTD versus Δt [see Eq. (16)].

in Fig. 3, LTD occurs in an effective range of $\Delta t_l^* < \Delta t < \Delta t_r^*$. We note that a peak exists at $t_0 = 80$ msec, and hence peak LTD occurs when PF firing precedes CF firing by 80 msec. A CF firing causes LTD in conjunction with earlier PF firings in the black region ($0 < \Delta t < \Delta t_l^*$), and it also gives rise to another LTD in association with later PF firings in the gray region ($\Delta t_l^* < \Delta t < 0$). The effect of CF firing on earlier PF firings is much larger than that on later PF firings. However, outside the effective range (i.e., $\Delta t > \Delta t_r^*$ or $< \Delta t_l^*$), PF firings alone leads to LTP, due to absence of effectively associated CF firings.

F. Numerical Method for Integration

Numerical integration of the governing Eq. (3) for the time-evolution of states of individual neurons, along with the update rule for synaptic plasticity of Eq. (12), is done by employing the 2nd-order Runge-Kutta method with the time step 1 msec. For each realization, we choose random initial points $v_i^{(X)}(0)$ for the i th neuron in the X population with uniform probability in the range of $v_i^{(X)}(0) \in (V_L^{(X)} - 5.0, V_L^{(X)} + 5.0)$; the values of $V_L^{(X)}$ are given in Table I.

III. EFFECT OF DIVERSE SPIKING PATTERNS OF GR CLUSTERS ON MOTOR LEARNING FOR THE OKR ADAPTION

In this section, we study the effect of diverse recoding of GR cells on motor learning for the OKR adaptation by varying the connection probability p_c from the GO to the GR cells. We mainly consider an optimal case of $p_c^* = 0.06$ where the spiking patterns of GR clusters are the most diverse. In this case, we first make dynamical classification of diverse spiking patterns of the GR clusters. Then, we investigate the effect of diverse spiking patterns on the synaptic plasticity at the PF-PC synapses and the subsequent learning process in the PC-VN-IO system. Finally, we vary p_c from the optimal

value p_c^* , and study dependence of the diversity degree \mathcal{D} of spiking patterns and the saturated learning gain degree \mathcal{L}_g^* on p_c . Both \mathcal{D} and \mathcal{L}_g^* are found to form bell-shaped curves with peaks at p_c^* , and they have strong correlation with the Pearson's coefficient $r \simeq 0.9998$. As a result, the more diverse in recording of GR cells, the more effective in the motor learning for the OKR adaptation.

A. Firing Activity in The Whole Population of GR Cells

As shown in Fig. 2, recoding process is performed in the granular layer (corresponding to the input layer of the cerebellar cortex), consisting of GR and GO cells. In the GR-GO feedback system, GR cells (principal output cells in the granular layer) receive excitatory context signals for the post-eye-movement via the sinusoidally-modulating MFs [see Fig. 1(b1)] and make recoding of context signals. In this recoding process, GO cells make effective inhibitory coordination for diverse recoding of GR cells. Thus, diversely recoded signals are fed into the PCs (principal output cells in the cerebellar cortex) via PFs. Due to this type of diverse recoding of GR cells, the cerebellum was recently reinterpreted as a liquid state machine with powerful discriminating/separating capability (i.e., different input signals are transformed into more different ones via recoding process) rather than the simple perceptron in the Marr-Albus-Ito theory [67, 68].

We first consider the firing activity in the whole population of GR cells for $p_c^* = 0.06$. Collective firing activity may be well visualized in the raster plot of spikes which is a collection of spike trains of individual neurons. Such raster plots of spikes are fundamental data in experimental neuroscience. As a population quantity showing collective firing behaviors, we use an instantaneous whole-population spike rate $R_{GR}(t)$ which may be obtained from the raster plots of spikes [37–44]. To obtain a smooth instantaneous whole-population spike rate, we employ the kernel density estimation (kernel smoother) [69]. Each spike in the raster plot is convoluted (or blurred) with a kernel function $K_h(t)$ [such as a smooth Gaussian function in Eq. (18)], and then a smooth estimate of instantaneous whole-population spike rate $R_{GR}(t)$ is obtained by averaging the convoluted kernel function over all spikes of GR cells in the whole population:

$$R_{GR}(t) = \frac{1}{N} \sum_{i=1}^N \sum_{s=1}^{n_i} K_h(t - t_s^{(i)}), \quad (17)$$

where $t_s^{(i)}$ is the s th spiking time of the i th GR cell, n_i is the total number of spikes for the i th GR cell, and N is the total number of GR cells (i.e., $N = N_c \cdot N_{GR} = 51, 200$). Here, we use a Gaussian kernel function of band width h :

$$K_h(t) = \frac{1}{\sqrt{2\pi}h} e^{-t^2/2h^2}, \quad -\infty < t < \infty. \quad (18)$$

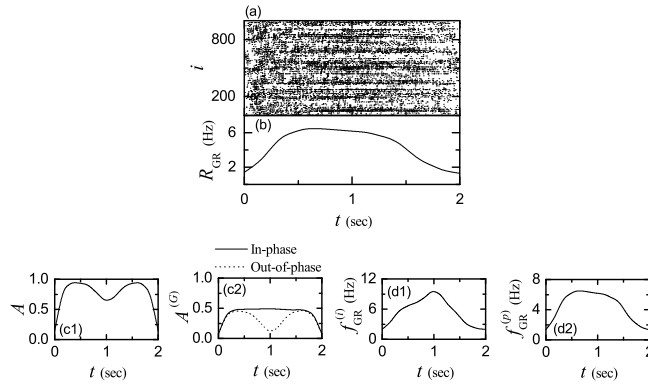


FIG. 4: Firing activity of GR cells in an optimal case of p_c (connection probability from GO to GR cells) = 0.06. (a) Raster plots of spikes of 10^3 randomly chosen GR cells. (b) Instantaneous whole-population spike rate $R_{GR}(t)$ in the whole population of GR cells. Band width for $R_{GR}(t)$: $h = 10$ msec. Plots of the activation degrees (c1) A in the whole population of GR cells and (c2) $A^{(G)}$ in the G spiking group [G : in-phase (solid curve) and out-of-phase (dotted curve)]. Plots of (d1) instantaneous individual firing rate $f_{GR}^{(i)}(t)$ for the active GR cells and (d2) instantaneous population spike rate $f_{GR}^{(p)}(t)$ for the whole population of GR cells. Bin size for (c1)-(d2): $\Delta t = 10$ msec.

Throughout the paper, the band width h of $K_h(t)$ is 10 msec.

Figure 4(a) shows a raster plot of spikes of 10^3 randomly chosen GR cells. At the initial and the final stages of the cycle, GR cells fire sparse spikes, because the firing rates of Poisson spikes for the MF are low. On the other hand, at the middle stage, the firing rates for the MF are relatively high, and hence spikes of GR cells become relatively dense. Figure 4(b) shows the instantaneous whole-population spike rate $R_{GR}(t)$ in the whole population of GR cells. $R_{GR}(t)$ is basically in proportion to the sinusoidally-modulating inputs via MFs. However, it has a different waveform with a central plateau. At the initial stage, it rises rapidly, then a broad plateau appears at the middle stage, and at the final stage, it decreases slowly. In comparison to the MF signal, the top part of $R_{GR}(t)$ becomes lowered and flattened, due to the effect of inhibitory GO cells. Thus, a central plateau emerges.

We next consider the activation degree of GR cells. To examine it, we divide the whole learning cycle (2000 msec) into 200 bins (bin size: 10 msec). Then, we get the activation degree A_i for the active GR cells in the i th bin:

$$A_i = \frac{N_{a,i}}{N}, \quad (19)$$

where $N_{a,i}$ and N are the number of active GR cells in the i th bin and the total number of GR cells, respectively. Figure 4(c1) shows a plot of the activation degree $A(t)$ in the whole population of GR cells. It is nearly symmetric, and has double peaks with a central valley at the middle

stage; its values at both peaks are about 0.94 and the central minimum value is about 0.65.

Presence of the central valley in $A(t)$ is in contrast to the central plateau in $R_{GR}(t)$. Appearance of such a central valley may be understood as follows. The whole population of GR cells can be decomposed into two types of in-phase and out-of-phase spiking groups. Spiking patterns of in-phase (out-of-phase) GR cells are in-phase (out-of-phase) with respect to $R_{GR}(t)$ (representing the population-averaged firing activity in the whole population of GR cells); details will be given in Figs. 5 and 6. Then, the activation degree $A_i^{(G)}$ of active GR cells in the G spiking group in the i th bin is given by:

$$A_i^{(G)} = \frac{N_{a,i}^{(G)}}{N}, \quad (20)$$

where $N_{a,i}^{(G)}$ is the number of active GR cells in the G spiking group (G : in-phase or out-of-phase) in the i th bin. The sum of $A_i^{(G)}(t)$ over the in- and the out-of-phase spiking groups is just the activation degree $A_i(t)$ in the whole population. Figure 4(c2) shows plots of activation degree $A^{(G)}(t)$ in the in-phase (solid line) and the out-of-phase (dotted curve) spiking groups. In the case of in-phase spiking group, $A^{(G)}(t)$ has a central plateau, while $A^{(G)}(t)$ has double peaks with a central valley in the case of out-of-phase spiking group. Hence, small contribution of out-of-phase spiking group at the middle stage leads to emergence of the central valley in $A(t)$ in the whole population.

We note again that, in the whole population the activation degree $A(t)$ with a central valley is in contrast to $R_{GR}(t)$ with a central plateau. To understand this discrepancy, we consider the bin-averaged instantaneous individual firing rates $f_{GR}^{(i)}$ of active GR cells:

$$f_{GR}^{(i)} = \frac{N_{s,i}}{N_{a,i} \Delta t}, \quad (21)$$

where $N_{s,i}$ is the number of spikes of GR cells in the i th bin, $N_{a,i}$ is the number of active GR cells in the i th bin, and the bin size Δt is 10 msec. Figure 4(d1) shows a plot of $f_{GR}^{(i)}(t)$ for the active GR cells. We note that active GR cells fire spikes at higher firing rates at the middle stage because $f_{GR}^{(i)}(t)$ has a central peak. Then, the bin-averaged instantaneous population spike rate $f_{GR}^{(p)}$ is given by the product of the activation degree of Eq. (19) and the instantaneous individual firing rate of Eq. (21):

$$f_{GR}^{(p)} = A_i f_{GR}^{(i)} = \frac{N_{s,i}}{N \Delta t}. \quad (22)$$

The instantaneous population spike rate $f_{GR}^{(p)}(t)$ in Fig. 4(d2) has a central plateau, as in the case of $R_{GR}(t)$. We note that both $f_{GR}^{(p)}(t)$ and $R_{GR}(t)$ correspond to bin-based estimate and kernel-based smooth estimate for the instantaneous whole-population spike rate for the GR

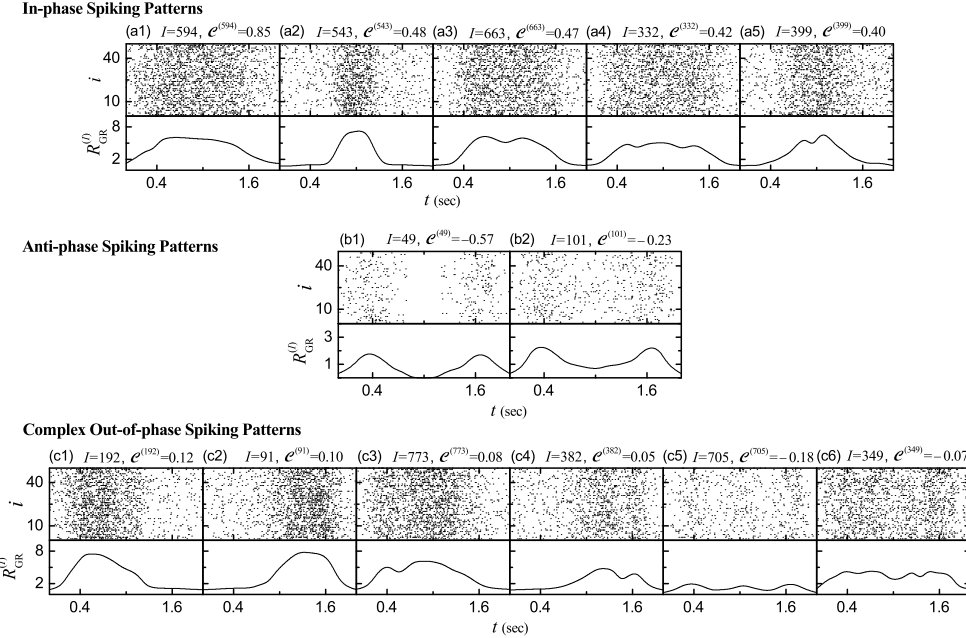


FIG. 5: Diverse spiking patterns in the GR clusters in the optimal case of $p_c^* = 0.06$. Raster plots of spikes and instantaneous cluster spike rates $R_{\text{GR}}^{(I)}(t)$ for diverse spiking patterns. Five in-phase spiking patterns in the I th GR clusters; $I =$ (a1) 594, (a2) 543, (a3) 663, (a4) 332, and (a5) 399. Two anti-phase spiking patterns in the I th GR cluster; $I =$ (b1) 49 and (b2) 101. Six complex out-of-phase spiking patterns in the I th GR clusters; $I =$ (c1) 192, (c2) 91, (c3) 773, (c4) 382, (c5) 705, and (c6) 349. $C^{(I)}$ represents the conjunction index of the spiking pattern in the I th GR cluster.

cells, respectively [37]. In this way, although the activation degree $A(t)$ of GR cells are lower at the middle stage, their population spike rate becomes nearly the same as that in the neighboring parts (i.e., central plateau is formed), due to the higher individual firing rates.

B. Dynamical Classification of Spiking Patterns of GR Clusters

There are $N_C (= 2^{10})$ GR clusters. $N_{\text{GR}} (= 50)$ GR cells in each GR cluster share the same inhibitory and excitatory inputs via their dendrites which synaptically contact the two glomeruli (i.e., terminals of MFs) at both ends of the GR cluster [see Fig. 2(b)]; nearby inhibitory GO cell axons innervate the two glomeruli. Hence, GR cells in each GR cluster show similar firing behaviors. Similar to the case of $R_{\text{GR}}(t)$ in Eq. (17), the firing activity of the I th GR cluster is characterized in terms of its instantaneous cluster spike rate $R_{\text{GR}}^{(I)}(t)$ ($I = 1, \dots, N_C$):

$$R_{\text{GR}}^{(I)}(t) = \frac{1}{N_{\text{GR}}} \sum_{i=1}^{N_{\text{GR}}} \sum_{s=1}^{n_i^{(I)}} K_h(t - t_s^{(I,i)}), \quad (23)$$

where $t_s^{(I,i)}$ is the s th spiking time of the i th GR cell in the I th GR cluster and $n_i^{(I)}$ is the total number of spikes for the i th GR cell in the I th GR cluster.

We introduce the conjunction index $C^{(I)}$ of each GR cluster, representing the degree for the conjunction (association) of the spiking behavior $[R_{\text{GR}}^{(I)}(t)]$ of each I th GR cluster with that of the whole population $[R_{\text{GR}}(t)]$ in Fig. 4(b) [i.e., denoting the degree for the resemblance (similarity) between $R_{\text{GR}}^{(I)}(t)$ and $R_{\text{GR}}(t)$]. The conjunction index $C^{(I)}$ is given by the cross-correlation at the zero-time lag [i.e., $\text{Corr}_{\text{GR}}^{(I)}(0)$] between $R_{\text{GR}}^{(I)}(t)$ and $R_{\text{GR}}(t)$:

$$\text{Corr}_{\text{GR}}^{(I)}(\tau) = \frac{\overline{\Delta R_{\text{GR}}(t + \tau) \Delta R_{\text{GR}}^{(I)}(t)}}{\sqrt{\Delta R_{\text{GR}}^2(t)} \sqrt{\Delta R_{\text{GR}}^{(I)}(t)^2}}, \quad (24)$$

where $\Delta R_{\text{GR}}(t) = R_{\text{GR}}(t) - \overline{R_{\text{GR}}(t)}$, $\Delta R_{\text{GR}}^{(I)}(t) = R_{\text{GR}}^{(I)}(t) - \overline{R_{\text{GR}}^{(I)}(t)}$, and the overline denotes the time average. We note that $C^{(I)}$ represents well the phase difference (shift) between the spiking patterns $[R_{\text{GR}}^{(I)}(t)]$ of GR clusters and the firing behavior $[R_{\text{GR}}(t)]$ in the whole population.

Figure 5 shows diverse spiking patterns of GR clusters. This type of diversity arises from inhibitory coordination of GO cells on the firing activity of GR cells in the GR-GO feedback system in the granular layer. Five examples for “in-phase” spiking patterns in the I th ($I = 594, 543, 663, 332$, and 399) GR clusters are given in Figs. 5(a1)-5(a5), respectively. Raster plot of spikes of $N_{\text{GR}} (= 50)$ GR cells and the corresponding instanta-

neous cluster spike rate $R_{\text{GR}}^{(I)}(t)$ are shown, along with the value of $\mathcal{C}^{(I)}$ in each case of the I th GR cluster. In all these cases, the instantaneous cluster spike rates $R_{\text{GR}}^{(I)}(t)$ are in-phase relative to the instantaneous whole-population spike rate $R_{\text{GR}}(t)$. Among them, in the case of $I = 594$ with the highest $\mathcal{C}^{(I)}$ ($= 0.85$), $R_{\text{GR}}^{(594)}(t)$ with a central plateau is the most similar (in-phase) to $R_{\text{GR}}(t)$. In the next case of $I = 543$ with $\mathcal{C}^{(I)} = 0.48$, $R_{\text{GR}}^{(543)}(t)$ has a central sharp peak, and hence its similarity degree relative to $R_{\text{GR}}(t)$ decreases. The remaining two cases of $I = 663$ and 332 (with more than one central peaks) may be regarded as ones developed from the case of $I = 594$. With increasing the number of peaks in the central part, the value of $\mathcal{C}^{(I)}$ decreases, and hence the resemblance degree relative to $R_{\text{GR}}(t)$ is reduced. The final case of $I = 399$ with double peaks can be considered as one evolved form the case of $I = 543$. In this case, the value of $\mathcal{C}^{(I)}$ is reduced to 0.40 . All the GR clusters, exhibiting in-phase spiking patterns, constitute the in-phase spiking group where the range of $\mathcal{C}^{(I)}$ is found to be $(0.39, 0.85)$.

Two examples for “anti-phase” spiking patterns in the I th ($I = 49$ and 101) GR clusters are given in Figs. 5(b1) and 5(b2), respectively. In both cases, the instantaneous cluster spike rates $R_{\text{GR}}^{(I)}(t)$ are anti-phase with respect to $R_{\text{GR}}(t)$ in the whole population. In the case of $I = 49$ with the lowest $\mathcal{C}^{(I)}$ ($= -0.57$), $R_{\text{GR}}^{(49)}(t)$ is the most anti-phase to $R_{\text{GR}}(t)$, and it has double peaks near the 1st and the 3rd quartiles and a central deep valley at the middle of the cycle. The case of $I = 101$ with $\mathcal{C}^{(I)}$ ($= -0.23$) may be regarded as evolved from the case of $I = 49$. It has an increased (but still negative) value of $\mathcal{C}^{(I)}$ ($= -0.23$) due to the risen central shallow valley. All the GR clusters, exhibiting anti-phase spiking patterns, form the anti-phase spiking group where the range of $\mathcal{C}^{(I)}$ is found to be $(-0.57, -0.20)$.

A 3rd type of complex “out-of-phase” spiking patterns with $-0.20 < \mathcal{C}^{(I)} < 0.39$ also exist between the in-phase and the anti-phase spiking patterns. Figure 5(c1)-5(c6) show six examples for the complex out-of-phase spiking patterns in the I th ($I = 192, 91, 773, 382, 705$, and 349) GR clusters. The cases of $I = 192$ and 91 seem to be developed from the in-phase spiking pattern in the I th ($I = 594$ or 543) GR cluster. In the case of $I = 192$, $R_{\text{GR}}^{(192)}$ has a left-skewed peak near the 1st quartile of the cycle, while in the case of $I = 91$, $R_{\text{GR}}^{(91)}$ has a right-skewed peak near the 3rd quartile. Hence, the values of $\mathcal{C}^{(I)}$ for $I = 192$ and 91 are reduced to 0.12 and 0.10 , respectively. In the next two cases of $I = 773$ and 382 , they seem to be developed from the cases of $I = 192$ and 91 , respectively. The left-skewed (right-skewed) peak in the case of $I = 192$ (91) is bifurcated into double peaks, which leads to more reduction of conjunction indices; $\mathcal{C}^{(773)} = 0.08$ and $\mathcal{C}^{(382)} = 0.05$. In the remaining case of $I = 705$, it seems to be evolved from the anti-phase spiking pattern in the $I = 101$ case. The central valley for $I = 101$ is transformed into a central peak. Thus, $R_{\text{GR}}^{(705)}$ has three

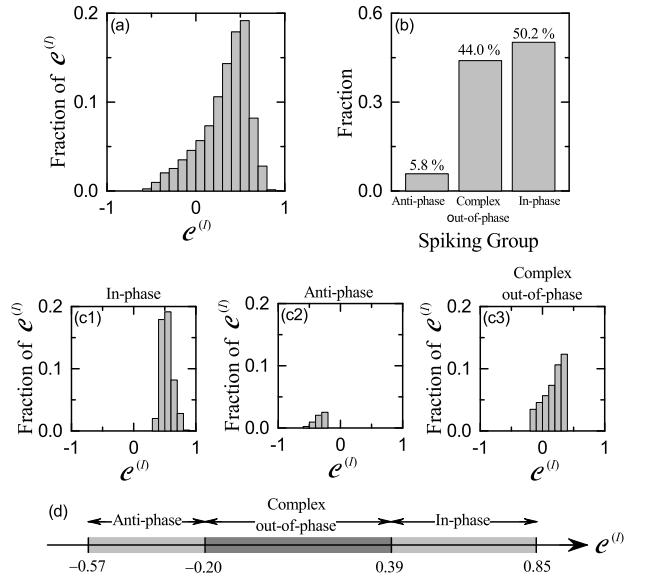


FIG. 6: Characterization of diverse spiking patterns in the GR clusters in the optimal case of $p_c^* = 0.06$. (a) Distribution of conjunction indices $\{\mathcal{C}^{(I)}\}$ for the GR clusters in the whole population. (b) Fraction of spiking groups. Distribution of conjunction indices $\{\mathcal{C}^{(I)}\}$ for the (c1) in-phase, (c2) anti-phase, and (c3) complex out-of-phase spiking groups. Bin size for the histograms in (a) and in (c1)-(c3) is 0.1 . (d) Bar diagram for the ranges of conjunction indices $\{\mathcal{C}^{(I)}\}$ for the in-phase, anti-phase, and complex out-of-phase spiking groups.

peaks, and its value of $\mathcal{C}^{(705)}$ is a little increased to -0.18 . As $\mathcal{C}^{(I)}$ is more increased toward the zero, $R_{\text{GR}}^{(I)}$ becomes more complex, as shown in Fig. 5(c6) in the case of $I = 349$ with $\mathcal{C}^{(349)} = -0.07$.

Results on characterization of the diverse in-, anti-, and complex out-of-phase spiking patterns are shown in Fig. 6. Figure 6(a) shows the plot of the fraction of conjunction indices $\mathcal{C}^{(I)}$ in the whole GR clusters. $\mathcal{C}^{(I)}$ increases slowly from the negative to the peak at 0.55 , and then it decreases rapidly. For this distribution of $\{\mathcal{C}^{(I)}\}$, the range is $(-0.57, 0.85)$, the mean is 0.32 , and the standard deviation is 0.516 . Then, the diversity degree \mathcal{D} for the spiking patterns $[R_{\text{GR}}^{(I)}(t)]$ of all the GR clusters is given by:

$$\mathcal{D} = \text{Relative Standard Deviation} \quad \text{for the Distribution of } \{\mathcal{C}^{(I)}\}, \quad (25)$$

where the relative standard deviation is just the standard deviation divided by the mean. In the optimal case of $p_c^* = 0.06$, $\mathcal{D}^* \simeq 1.613$, which is just a quantitative measure for the diverse recoding performed via feedback cooperation between the GR and the GO cells in the granular layer. As will be seen later in Fig. 17(b) for the plot of \mathcal{D} versus p_c , \mathcal{D}^* is the maximum, and hence spiking patterns of GR clusters at p_c^* is the most diverse.

We decompose the whole GR clusters into the in-, anti-, and complex out-of-phase spiking groups. Figure 6(b)

shows the fraction of spiking groups. The in-phase spiking group is a major one with fraction 50.2%, while the anti-phase spiking group is a minor one with fraction 5.8%. Between them, the complex out-of-phase spiking group with fraction 44% exists. In this case, the spiking-group ratio, given by the ratio of the fraction of the in-phase spiking group to that of the out-of-phase spiking group (consisting of both the anti- and complex out-of-phase spiking groups), is $\mathcal{R}^* \simeq 1.008$. Thus, in the optimal case of $p_c^* = 0.06$, the fractions between the in- and the out-of-phase spiking groups are well balanced. Under such good balance between the in- and the out-of-phase spiking groups, spiking patterns of the GR clusters are the most diverse.

Figures 6(c1)-6(c3) also show the plots of conjunction indices $\mathcal{C}^{(I)}$ of the GR clusters in the in-, anti-, and complex out-of-phase spiking groups, respectively. The ranges for the distributions of $\mathcal{C}^{(I)}$ in the three spiking groups are also given in the bar diagram in Fig. 6(d). In the case of in-phase spiking group, the distribution of $\mathcal{C}^{(I)}$ with a peak at 0.55 has only positive values in the range of (0.39, 0.85), and its mean and standard deviations are 0.538 and 0.181, respectively. On the other hand, in the case of the anti-phase spiking group, the distribution of $\mathcal{C}^{(I)}$ with a peak at -0.25 has only negative values in the range of (-0.57, -0.20), and its mean and standard deviations are -0.331 and 0.135, respectively. Between the in- and the anti-phase spiking groups, there exists an intermediate complex out-of-phase spiking group. In this case, the range for the distribution of $\mathcal{C}^{(I)}$ with a peak at 0.35 is (-0.20, 0.39), and the mean and the standard deviation are 0.174 and 0.242, respectively. As will be seen in the next subsection, these in-, anti-, and complex out-of-phase spiking groups play their own roles in the synaptic plasticity at PF-PC synapses, respectively.

C. Effect of Diverse Recoding in GR Clusters on Synaptic Plasticity at PF-PC Synapses

Based on dynamical classification of spiking patterns of GR clusters, we investigate the effect of diverse recoding in the GR clusters on synaptic plasticity at PF-PC synapses. As shown in the above subsection, MF context input signals for the post-eye-movement are diversely recoded in the granular layer (corresponding to the input layer of the cerebellar cortex). The diversely-recoded in- and out-of-phase PF (student) signals (corresponding to the outputs from the GR cells) are fed into the PCs (i.e., principal cells of the cerebellar cortex) and the BCs in the Purkinje-molecular layer (corresponding to the output layer of the cerebellar cortex). The PCs also receive in-phase error-teaching CF (instructor) signals from the IO, along with the inhibitory inputs from the BCs. Then, the synaptic weights at the PF-PC synapses vary depending on the relative phase difference between the PF (student) signals and the CF (instructor) signals.

We first consider the change in normalized synaptic

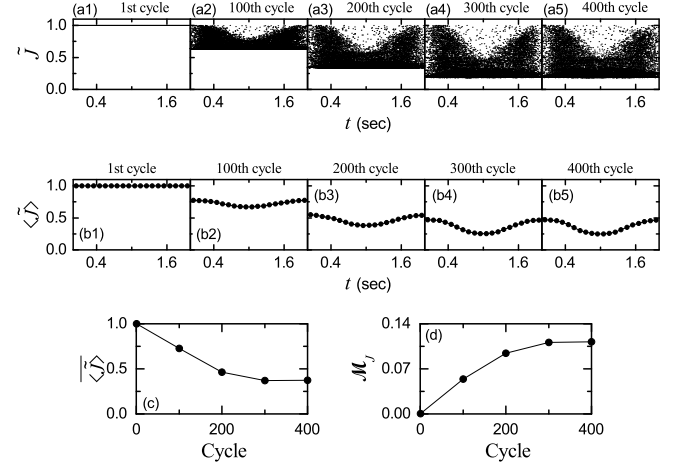


FIG. 7: Change in synaptic weights of active PF-PC synapses during learning in the optimal case of $p_c^* = 0.06$. (a1)-(a5) Cycle-evolution of distribution of normalized synaptic weights \tilde{J} of active PF signals. (b1)-(b5) Cycle-evolution of bin-averaged (normalized) synaptic weights $\langle \tilde{J} \rangle$ of active PF signals. Bin size: $\Delta t = 100$ msec. Plots of (c) cycle-averaged mean $\langle \tilde{J} \rangle$ and (d) modulation \mathcal{M}_J for $\langle \tilde{J} \rangle$ versus cycle.

weights \tilde{J} of active PF-PC synapses during learning in the optimal case of $p_c^* = 0.06$;

$$\tilde{J}(t) = \frac{J_{ij}^{(\text{PC,PF})}(t)}{J_0^{(\text{PC,PF})}}, \quad (26)$$

where the initial synaptic strength ($J_0^{(\text{PC,PF})} = 0.006$) is the same for all PF-PC synapses. Figures 7(a1)-7(a5) show cycle-evolution of distribution of \tilde{J} of active PF-PC synapses. With increasing the learning cycle, normalized synaptic weights \tilde{J} are decreased due to LTD at PF-PC synapses, and eventually their distribution seems to be saturated at about the 300th cycle. We note that in-phase PF signals are strongly depressed by the in-phase CF signals, while out-of-phase PF signals are weakly depressed due to the phase difference between the PF and the CF signals. As shown in Fig. 4(c2), the activation degree $A^{(G)}$ of the in-phase spiking group is dominant at the middle stage of the cycle, while at the other parts of the cycle, the activation degrees of the in- and the out-of-phase spiking groups are comparable. Consequently, strong LTD occurs at the middle stage, while at the initial and final stages weak LTD takes place.

To more clearly examine the above cycle evolutions, we get the bin-averaged (normalized) synaptic weight in each i th bin (bin size: $\Delta t = 100$ msec):

$$\langle \tilde{J}(t) \rangle_i = \frac{1}{N_{s,i}} \sum_{f=1}^{N_{s,i}} \tilde{J}_{i,f}(t), \quad (27)$$

where $\tilde{J}_{i,f}$ is the normalized synaptic weight of the f th active PF signal in the i th bin, and $N_{s,i}$ is the total num-

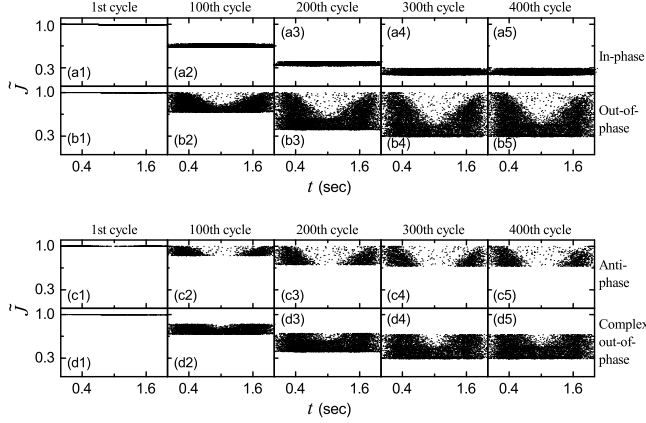


FIG. 8: Change in synaptic weights of active PF-PC synapses in each spiking group during learning in the optimal case of $p_c^* = 0.06$. Cycle-evolution of distributions of normalized synaptic weights $\tilde{J}^{(G)}$ of active PF signals in the G spiking group [G: (a1)-(a5) in-phase and (b1)-(b5) out-of-phase]. Cycle-evolution of distributions of normalized synaptic weights $\tilde{J}^{(G)}$ of active out-of-phase PF signals in the G spiking group [G: (c1)-(c5) anti-phase and (d1)-(d5) complex out-of-phase].

ber of active PF signals in the i th bin. Figures 7(b1)-7(b5) show cycle-evolution of bin-averaged (normalized) synaptic weights $\langle \tilde{J}(t) \rangle$ of active PF signals. In each cycle, $\langle \tilde{J}(t) \rangle$ forms a well-shaped curve. With increasing the cycle, the well curve comes down, its modulation [= (maximum - minimum)/2] increases, and saturation seems to occur at about the 300th cycle.

We also get the cycle-averaged mean $\overline{\langle \tilde{J}(t) \rangle}$ via time average of $\langle \tilde{J}(t) \rangle$ over a cycle:

$$\overline{\langle \tilde{J} \rangle} = \frac{1}{N_b} \sum_{i=1}^{N_b} \langle \tilde{J}(t) \rangle_i, \quad (28)$$

where N_b is the number of bins for cycle averaging, and the overbar represents the time average. Figures 7(c) and 7(d) show plots of the cycle-averaged mean $\overline{\langle \tilde{J}(t) \rangle}$ and the modulation \mathcal{M}_J for $\langle \tilde{J}(t) \rangle$ versus cycle. The cycle-averaged mean $\overline{\langle \tilde{J}(t) \rangle}$ decreases from 1 to 0.372 due to LTD at PF-PC synapses. However, strength of the LTD varies depending on the stages of the cycle. At the middle stage, strong LTD occurs, due to dominant contribution of in-phase active PF signals. On the other hand, at the initial and the final stages, weak LTD takes place, because of relatively comparable contributions of in- and out-of-phase active PF signals. As a result, with increasing cycle, the middle-stage part comes down more rapidly than the initial and final parts, and hence the modulation \mathcal{M}_J increases from 0 to 0.112.

We now decompose the whole active PF signals into the in- and the out-of-phase active PF signals, and make an intensive investigation on their effect on synaptic plasticity at PF-PC synapses. Figure 8 shows cycle-evolution

of distributions of normalized synaptic weights $\tilde{J}^{(G)}$ of active PF signals in the G spiking group [G: (a1)-(a5) in-phase and (b1)-(b5) out-of-phase] in the optimal case of $p_c^* = 0.06$; the out-of-phase spiking group consists of the anti- and the complex out-of-phase spiking groups. With increasing learning cycle, normalized synaptic weights $\tilde{J}^{(G)}$ for the in- and the out-of-phase PF signals are decreased, and saturated at about the 300th cycle. In the case of in-phase PF signals, they are strongly depressed via strong LTD at PF-PC synapses, and form the bottom dense parts in Figs. 7(a1)-7(a5). On the other hand, in the case of out-of-phase PF signals, they are weakly depressed through weak LTD at PF-PC synapses, and constitute the upper sparse parts in Figs. 7(a1)-7(a5). In this way, effective depression at PF-PC synapses occurs, depending on the spiking type (in or out-of-phase) of the active PF signals, which leads to a big modulation for the change in synaptic weights of the PF-PC synapses.

We also make further decomposition of the out-of-phase PF signals into the anti- and the complex out-of-phase ones. Figure 8 also shows cycle-evolution of distributions of normalized synaptic weights $\tilde{J}^{(G)}$ of active out-of-phase PF signals in the G spiking group [G: (c1)-(c5) anti-phase and (d1)-(d5) complex out-of-phase]. As the learning cycle is increased, normalized synaptic weights for the anti- and the complex out-of-phase PF signals are decreased and saturated at about the 300th cycle. In the case of anti-phase PF signals, weak depression occurs, and they constitute the top part for the out-of-phase PF signals in Figs. 8(b1)-8(b5). On the other hand, in the case of complex out-of-phase PF signals, intermediate LTD takes place, and they form the bottom part for the out-of-phase PF signals in Figs. 8(b1)-8(b5).

Figures 9(a1)-9(a5) show cycle-evolutions of bin-averaged (normalized) synaptic weights $\langle \tilde{J}^{(G)}(t) \rangle$ of active PF signals in the G spiking-group [i.e., corresponding to the bin-averages for the distributions of $\tilde{J}^{(G)}(t)$ in Figs. 8(a1)-8(a5) and Figs. 8(b1)-8(b5)]; G : in-phase (solid circles) and out-of-phase (open circles). In the case of in-phase PF signals, they are strongly depressed without modulation. On the other hand, in the case of out-of-phase PF signals, they are weakly depressed with modulation; at the initial and the final stages, they are more weakly depressed in comparison with the case at the middle stage.

The cycle-averaged means $\overline{\langle \tilde{J}^{(G)} \rangle}$ and modulations $\mathcal{M}_J^{(G)}$ for $\langle \tilde{J}^{(G)} \rangle$ are given in Figs. 9(b) and 9(c), respectively. Both cycle-averaged means in the cases of the in- and the out-of-phase PF signals decrease, and saturations occur at about the 300th cycle. In comparison with the case of out-of-phase PF signals (open circles), the cycle-averaged means in the case of in-phase PF signals (solid circles) are more reduced; the saturated limit value in the case of in-phase (out-of-phase) PF signals is 0.199 (0.529). In contrast, modulation occurs only for the out-of-phase PF signals (open circles), it increases with cycle, and becomes saturated at about the 300th

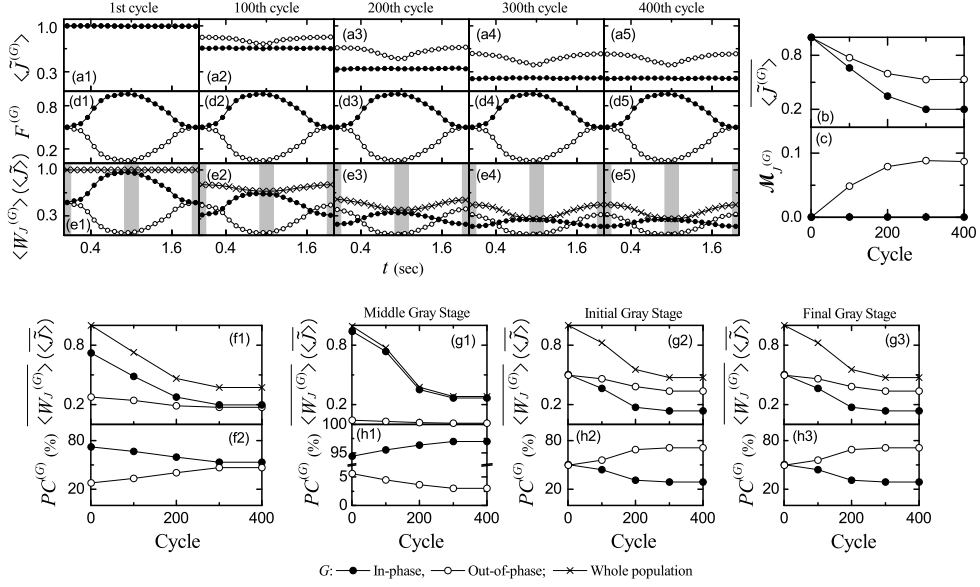


FIG. 9: Optimal case of $p_c^* = 0.06$. (a1)-(a5) Cycle-evolution of bin-averaged (normalized) synaptic weights $\langle \tilde{J}^{(G)} \rangle$ of active PF signals in the G spiking-group. Plots of (b) cycle-averaged mean $\langle \tilde{J}^{(G)} \rangle$ and (c) modulation $M_J^{(G)}$ for $\langle \tilde{J}^{(G)} \rangle$ versus cycle. (d1)-(d5) Cycle-evolution of firing fraction $F^{(G)}$ of active PF signals in the G spiking group. (e1)-(e5) Cycle-evolution of weighted bin-averaged synaptic weights $\langle W_J^{(G)} \rangle$ of active PF signals in the G spiking group; for comparison, bin-averaged synaptic weights $\langle \tilde{J} \rangle$ in the whole population of GR cells are also given. (f1) Plots of cycle-averaged means $\langle W_J^{(G)} \rangle$ and $\langle \tilde{J} \rangle$ for $\langle W_J^{(G)} \rangle$ and $\langle \tilde{J} \rangle$ versus cycle. (f2) Plots of percentage contributions $PC^{(G)}$ of the G spiking group (i.e., $\langle W_J^{(G)} \rangle / \langle \tilde{J} \rangle$) versus cycle. Left, right, and middle vertical gray bands in each cycle in (e1)-(e5) denote the initial, final, and middle stages, respectively. Plots of stage-averaged values $\langle W_J^{(G)} \rangle$ and $\langle \tilde{J} \rangle$ versus cycle at the (g1) middle, (g2) initial, and (g3) final stages of a cycle. Plots of percentage contributions $PC^{(G)}$ of the G spiking group versus cycle at the (h1) middle, (h2) initial, and (h3) final stages of a cycle.

cycle where the saturated value is 0.087.

In addition to the above bin-averaged (normalized) synaptic weights $\langle \tilde{J}^{(G)}(t) \rangle$, we need another information on firing fraction $F^{(G)}(t)$ of active PF signals in the G (in- or out-of-phase) spiking group to obtain the contribution of each spiking group to the bin-averaged synaptic weights $\langle \tilde{J}(t) \rangle$ of active PF signals in the whole population. The firing fraction $F_i^{(G)}$ of active PF signals in the G spiking group in the i th bin is given by:

$$F_i^{(G)} = \frac{N_{s,i}^{(G)}}{N_{s,i}}, \quad (29)$$

where $N_{s,i}$ is the total number of active PF signals in the i th bin and $N_{s,i}^{(G)}$ is the number of active PF signals in the G spiking group in the i th bin. We note that $F^{(G)}(t)$ is the same, independently of the learning cycle, because firing activity of PF signals depends only on the GR and GO cells in the granular layer.

Figures 9(d1)-9(d5) show the firing fraction $F^{(G)}(t)$ of active PF signals in the G spiking group. The firing fraction $F^{(G)}(t)$ for the in-phase active PF signals (solid circles) forms a bell-shaped curve, while $F^{(G)}(t)$ for the out-of-phase active PF signals (open circles) forms a well-shaped curve. The bell-shaped curve for the in-phase PF

signal is higher than the well-shaped curve for the out-of-phase PF signal. For the in-phase PF signals, the firing fraction $F^{(G)}(t)$ is about 0.94 (i.e., $\sim 94\%$) at the middle stage, and about 0.51 (i.e., $\sim 51\%$) at the initial and the final stages. On the other hand, for the out-of-phase signals, about 0.49 (i.e., $\sim 49\%$) at the initial and the final stages, and about 0.06 (i.e., $\sim 6\%$) at the middle stage. Consequently, the fraction of in-phase active PF signals is dominant at the middle stage, while at the initial and the final stages, the fractions of both in- and out-of-phase active PF signals are nearly the same.

The weighted bin-averaged synaptic weight $\langle W_J^{(G)} \rangle_i$ for each G spiking group in the i th bin is given by the product of the firing fraction $F_i^{(G)}$ and the bin-averaged (normalized) synaptic weight $\langle \tilde{J}^{(G)} \rangle_i$:

$$\langle W_J^{(G)} \rangle_i = F_i^{(G)} \langle \tilde{J}^{(G)} \rangle_i, \quad (30)$$

where the firing fraction $F_i^{(G)}$ plays a role of a weighting function for $\langle \tilde{J}^{(G)} \rangle_i$. Then, the bin-averaged (normalized) synaptic weight $\langle \tilde{J} \rangle_i$ of active PF signals in the whole population in the i th bin [see Eq. (27)] is given by the sum of weighted bin-averaged synaptic weights

$\langle W_J^{(G)} \rangle_i$ of all spiking groups:

$$\langle \tilde{J} \rangle_i = \sum_G^{\text{all spiking groups}} \langle W_J^{(G)} \rangle_i. \quad (31)$$

Hence, $\langle W_J^{(G)}(t) \rangle$ represents contribution of the G spiking group to $\langle \tilde{J}(t) \rangle$ of active PF signals in the whole population.

Figures 9(e1)-9(e5) show cycle-evolution of weighted bin-averaged synaptic weights $\langle W_J^{(G)}(t) \rangle$ of active PF signals in the G spiking group [G : in-phase (solid circles) and out-of-phase (open circles)]. In the case of in-phase PF signals, the bin-averaged (normalized) synaptic weights $\langle \tilde{J}^{(G)} \rangle$ are straight horizontal lines, the firing fraction $F^{(G)}(t)$ is a bell-shaped curve, and hence their product leads to a bell-shaped curve for the weighted bin-averaged synaptic weight $\langle W_J^{(G)}(t) \rangle$. With increasing the cycle, the horizontal straight lines for $\langle \tilde{J}^{(G)}(t) \rangle$ come down rapidly, while there is no change with cycle in $F^{(G)}(t)$. Hence, the bell-shaped curves for $\langle W_J^{(G)}(t) \rangle$ also come down quickly, their modulations also are reduced in a fast way, and they become saturated at about the 300th cycle.

On the other hand, in the case of out-of-phase PF signals, the bin-averaged (normalized) synaptic weights $\langle \tilde{J}^{(G)}(t) \rangle$ lie on a well-shaped curve, the firing fraction $F^{(G)}(t)$ also is a well-shaped curve, and then their product results in a well-shaped curve for the weighted bin-averaged synaptic weight $\langle W_J^{(G)}(t) \rangle$. With increasing the cycle, the well-shaped curves for $\langle \tilde{J}^{(G)}(t) \rangle_i$ come down slowly, while there is no change with cycle in $F^{(G)}(t)$. Hence, the well-shaped curves for $\langle W_J^{(G)}(t) \rangle$ also come down gradually, their modulations also are reduced little by little, and eventually they get saturated at about the 300th cycle.

For comparison, bin-averaged (normalized) synaptic weights $\langle \tilde{J}(t) \rangle$ of active PF signals in the whole population (crosses) are also given in Figs. 9(e1)-9(e5), and they form a well-shaped curve. According to Eq. (31), the sum of the values at the solid circle (in-phase) and the open circle (out-of-phase) at a time t in each cycle is just the value at the cross (whole population). At the middle stage of each cycle, contributions of in-phase PF signals (solid circles) are dominant [i.e., contributions of out-of-phase PF signals (open circles) are negligible], while at the initial and the final stages, contributions of out-of-phase PF signals are larger than those of in-phase PF signals (both contributions must be considered). Consequently, $\langle \tilde{J}(t) \rangle$ of active PF signals in the whole population becomes more reduced at the middle stage than at the initial and the final stages, due to the dominant effect (i.e., strong LTD) of in-phase active PF signals at the middle stage, which results in a well-shaped curve for $\langle \tilde{J}(t) \rangle$ in the whole population.

We make a quantitative analysis for contribution of $\langle W_J^{(G)}(t) \rangle$ in each G spiking group to $\langle \tilde{J}(t) \rangle$ in the whole

population. Figure 9(f1) shows plots of cycle-averaged weighted synaptic weight $\overline{\langle W_J^{(G)}(t) \rangle}$ (i.e., time average of $\langle W_J^{(G)}(t) \rangle$ over a cycle) in the G spiking-group [G : in-phase (solid circles) and out-of-phase (open circles)] and cycle-averaged synaptic weight $\langle \tilde{J}(t) \rangle$ of Eq. (28) in the whole population (crosses) versus cycle. The cycle-averaged weighted synaptic weights $\overline{\langle W_J^{(G)}(t) \rangle}$ in the in-phase spiking group (solid circles) are larger than those in the out-of-phase spiking group (open circles), and their sums correspond to the cycle-averaged synaptic weight $\langle \tilde{J}(t) \rangle$ in the whole population (crosses). With increasing cycle, both $\overline{\langle W_J^{(G)}(t) \rangle}$ and $\overline{\langle \tilde{J}(t) \rangle}$ become saturated at about the 300th cycle. In the in-phase spiking group $\overline{\langle W_J^{(G)}(t) \rangle}$ decreases rapidly from 0.722 to 0.198, while $\overline{\langle W_J^{(G)}(t) \rangle}$ in the out-of-phase spiking group decreases slowly from 0.273 to 0.174. Thus, the saturated values of $\overline{\langle W_J^{(G)}(t) \rangle}$ in both the in- and the out-of-phase spiking groups become close.

The percentage contribution $PC^{(G)}$ of $\overline{\langle W_J^{(G)}(t) \rangle}$ in the G spiking group to $\overline{\langle \tilde{J}(t) \rangle}$ in the whole population is given by:

$$PC^{(G)}(\%) = \frac{\overline{\langle W_J^{(G)}(t) \rangle}}{\overline{\langle \tilde{J}(t) \rangle}} \times 100. \quad (32)$$

Figure 9(f2) shows a plot of $PC^{(G)}$ versus cycle [G : in-phase (solid circles) and out-of-phase (open circles)]. $PC^{(G)}$ of the in-phase spiking group decreases from 72.2 % to 53.2 %, while $PC^{(G)}$ of the out-of-phase spiking group increases from 27.3 % to 46.8 %. Thus, the saturated $PC^{(G)}$ of both the in- and the out-of-phase spiking groups get close.

We are particularly interested in the left, the right, and the middle vertical gray bands in each cycle in Figs. 9(e1)-9(e5) which denote the initial ($0 < t < 0.1$ sec), the final ($1.9 < t < 2.0$ sec), and the middle ($0.9 < t < 1.1$ sec) stages, respectively. In the case of in-phase (out-of-phase) spiking group, the maximum (minimum) of $\langle W_J^{(G)}(t) \rangle$ appears at the middle stage, while the minimum (maximum) occurs at the initial and the final stages. Figures 9(g1)-9(g3) show plots of stage-averaged weighted synaptic weight $\overline{\langle W_J^{(G)}(t) \rangle}$ [i.e., time average of $\langle W_J^{(G)}(t) \rangle$ over the stage] in the G spiking-group [G : in-phase (solid circles) and out-of-phase (open circles)] and stage-averaged synaptic weight $\overline{\langle \tilde{J}(t) \rangle}$ [i.e., time average of $\langle \tilde{J}(t) \rangle$ over the stage] in the whole population (crosses) versus cycle in the middle, the initial, and the final stages, respectively. The sum of the values of $\langle W_J^{(G)}(t) \rangle$ at a time t in the in- and the out-of-phase spiking groups corresponds to the value of $\langle \tilde{J}(t) \rangle$ in the whole population. As the cycle is increased, both $\overline{\langle W_J^{(G)}(t) \rangle}$ and $\overline{\langle \tilde{J}(t) \rangle}$ become saturated at about the 300th cycle. Figures 9(h1)-9(h3)

also show plots of percentage contribution $PC^{(G)}$ of the G spiking group (i.e., ratio of the stage-averaged weighted synaptic weight $\langle W_J^{(G)}(t) \rangle$ in the G spiking group to the stage-averaged synaptic weight $\langle \tilde{J}(t) \rangle$ in the whole population) in the middle, the initial, and the final stages, respectively; G : in-phase (solid circles) and out-of-phase (open circles).

In the case of in-phase spiking group, $\langle W_J^{(G)}(t) \rangle$ decreases rapidly with cycle in all the 3 stages, while in the case of out-of-phase spiking group, it also decreases in a relatively slow way with cycle. At the middle stage, $\langle W_J^{(G)}(t) \rangle$ in the in-phase spiking group (solid circles) is much higher than that in the out-of-phase spiking group (open circles), and it decreases rapidly from 0.944 to 0.266. In this case, the percentage contribution $PC^{(G)}$ of the in-phase spiking group increases from 94.4 % to 97.0 %. Consequently, the contribution of in-phase spiking group is dominant at the middle stage, which leads to strong LTD at the PF-PC synapses. On the other hand, at the initial and the final stages, with increasing cycle $\langle W_J^{(G)}(t) \rangle$ in the out-of-phase spiking group becomes larger than that in the in-phase spiking group. The percentage contribution $PC^{(G)}$ of the out-of-phase spiking group increases from 49.2 % to 70.2 %, while that of the in-phase spiking group decreases from 50.8 % to 29.8 %. As a result, the contribution of out-of-phase spiking group at the initial and the final stages is larger than that of in-phase spiking group, which results in weak LTD at the PF-PC synapses.

In the above way, under good balance between the in- and the out-of-phase spiking groups (i.e., spiking-group ratio $\mathcal{R}^* \simeq 1.008$) in the optimal case of $p_c^* = 0.06$, effective depression (i.e., strong/weak LTD) at the PF-PC synapses causes a big modulation in synaptic plasticity, which also leads to large modulations in firing activities of the PCs and the VN neuron (i.e., emergence of effective learning process). Hence, diverse recoding in the granular layer (i.e., appearance of diverse spiking patterns of GR clusters) which results in effective (strong/weak) LTD at the PF-PC synapses is essential for effective motor learning for the OKR adaptation, which will be discussed in the following subsection.

D. Effect of PF-PC Synaptic Plasticity on Subsequent Learning Process in The PC-VN-IO System

As a result of diverse recoding in the GR clusters, strong LTD occurs at the middle stage of a cycle due to dominant contribution of in-phase spiking group. On the other hand, at the initial and the final stages, weak LTD takes place due to larger contribution of out-of-phase spiking group. Due to this kind of effective (strong/weak) LTD at the PF-PC synapses, a big modulation in synaptic plasticity at the PF-PC synapses (i.e., big modula-

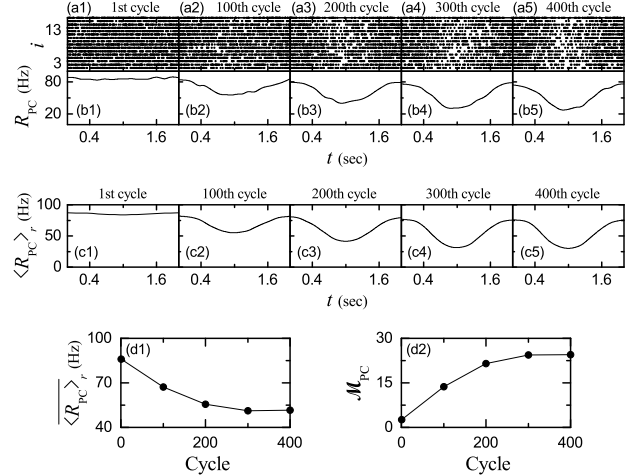


FIG. 10: Change in firing activity of PCs during learning in the optimal case of $p_c^* = 0.06$. (a1)-(a5) Raster plots of spikes of PCs and (b1)-(b5) instantaneous population spike rates $R_{PC}(t)$. (c1)-(c5) Realization-averaged instantaneous population spike rates $\langle R_{PC}(t) \rangle_r$; number of realizations is 100. Plots of (d1) cycle-averaged mean $\langle R_{PC}(t) \rangle_r$ and (d2) modulations \mathcal{M}_{PC} for $\langle R_{PC}(t) \rangle_r$ versus cycle.

tion in bin-averaged normalized synaptic weight $\langle \tilde{J}(t) \rangle$) emerges. In this subsection, we investigate the effect of PF-PC synaptic plasticity with a big modulation on the subsequent learning process in the PC-VN-IO system.

Figure 10 shows change in firing activity of PCs during learning in the optimal case of $p_c^* = 0.06$. Cycle-evolutions of raster plots of spikes of 16 PCs and the corresponding instantaneous population spike rates $R_{PC}(t)$ are shown in Figs. 10(a1)-10(a5) and Figs. 10(b1)-10(b5), respectively. Realization-averaged smooth instantaneous population spike rates $\langle R_{PC}(t) \rangle_r$ are also given in Figs. 10(c1)-10(c5); $\langle \dots \rangle_r$ denotes realization average and the number of realizations is 100. $\langle R_{PC}(t) \rangle_r$ seems to be saturated at about the 300th cycle.

With increasing the learning cycle, raster plots of spikes of all the 16 PCs become more and more sparse at the middle stage, which may be clearly in the instantaneous population spike rate $\langle R_{PC}(t) \rangle_r$. Due to the effect of synaptic plasticity at the PF-PC synapses, the minimum of $\langle R_{PC}(t) \rangle_r$ appears at the middle stage, while the maximum occurs at the initial and the final stages. Thus, the modulation of $\langle R_{PC}(t) \rangle_r$ increases with increasing the cycle.

In-phase PF (student) signals are strongly depressed by the in-phase CF (instructor) signals, while out-of-phase PF signals are weakly pressed due to the phase difference between the out-of-phase PF signals and the in-phase CF signals. Fraction of in-phase PF signals at the middle stage of a cycle is dominant. On the other hand, at the initial and the final stages, fraction of out-of-phase PF signals are larger than that of in-phase PF signals. Thus, bin-averaged normalized synaptic weights $\langle \tilde{J}(t) \rangle$ form a well-shaped curve, as shown in Figs. 7(b1)-7(b5).

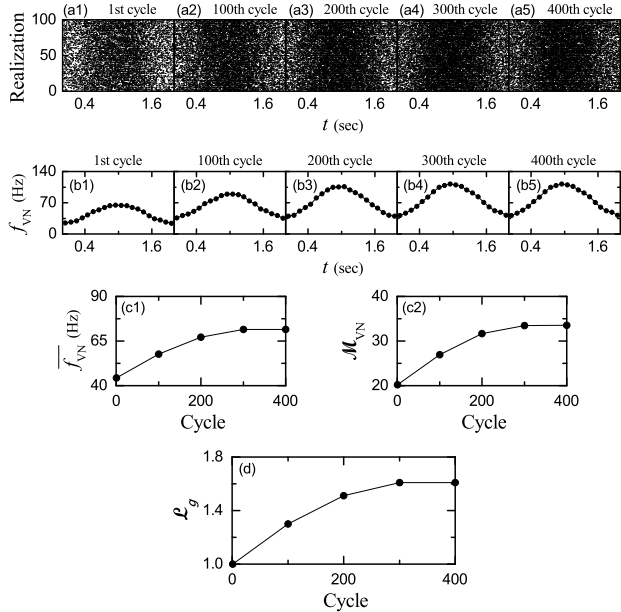


FIG. 11: Change in firing activity of the VN neuron during learning in the optimal case of $p_c^* = 0.06$. (a1)-(a5) Raster plots of spikes of the VN neuron (i.e., collection of spike trains for all the realizations; number of realizations is 100) and (b1)-(b5) bin-averaged instantaneous individual firing rate $f_{VN}(t)$; the bin size is $\Delta t = 100$ msec. Plots of (c1) cycle-averaged mean $\bar{f}_{VN}(t)$ and (c2) modulation M_{VN} for $f_{VN}(t)$ versus cycle. (d) Plot of learning gain degree \mathcal{L}_g versus cycle.

That is, strong LTD occurs at the middle stage, while at the initial and the final stages, weak LTD takes place. As a result of this kind of effective depression (strong/weak LTD) at the (excitatory) PF-PC synapses, $\langle R_{PC}(t) \rangle_r$ becomes lower at the middle stage (strong LTD) than at the initial and the final stages (weak LTD). Thus, $\langle R_{PC}(t) \rangle_r$ forms a well-shaped curve with a minimum at the middle stage.

Figures 10(d1) and 10(d2) show plots of cycle-averaged mean $\langle R_{PC}(t) \rangle_r$ (i.e., time average of $\langle R_{PC}(t) \rangle_r$ over the cycle) and modulation M_{PC} of $\langle R_{PC}(t) \rangle_r$ versus cycle, respectively. Due to LTD at the PF-PC synapses, the cycle-averaged mean $\langle R_{PC}(t) \rangle_r$ decreases monotonically from 86.1 Hz, and it becomes saturated at 51.7 Hz at about the 300th cycle. On the other hand, the modulation $\langle M_{PC} \rangle$ increases monotonically from 2.6 Hz, and it gets saturated at 24.1 Hz at about the 300th cycle. Consequently, a big modulation occurs in $\langle M_{PC} \rangle$ due to the effective depression (strong/weak LTD) at the PF-PC synapses. These PCs (principal cells of the cerebellar cortex) exert effective inhibitory coordination on the VN neuron which evokes OKR eye-movement.

Figure 11 shows change in firing activity of the VN neuron which produces the final output of the cerebellum during learning in the optimal case of $p_c^* = 0.06$. Cycle-evolutions of raster plots of spikes of the VN neuron (i.e., collection of spike trains for all the realizations; number

of realizations is 100) and the bin-averaged instantaneous individual firing rates $f_{VN}(t)$ (i.e., the number of spikes of the VN neuron in a bin with the bin width $\Delta t = 100$ msec) are shown in Figs. 11(a1)-11(a5) and Figs. 11(b1)-11(b5), respectively. $f_{VN}(t)$ seems to be saturated at about the 300th cycle.

In contrast to the case of PCs, as the cycle is increased, raster plots of spikes of the VN neuron become more and more dense at the middle stage, which may be clearly in the instantaneous individual firing rates $f_{VN}(t)$. Due to the effective inhibitory coordinations of PCs on the VN neuron, the maximum of $f_{VN}(t)$ appears at the middle stage, while the minimum occurs at the initial and the final stages. Thus, $f_{VN}(t)$ forms a bell-shaped curve.

Figures 11(c1) and 11(c2) show plots of cycle-averaged mean $\bar{f}_{VN}(t)$ of $f_{VN}(t)$ [i.e., time average of $f_{VN}(t)$ over the cycle] and modulation M_{VN} of $f_{VN}(t)$ versus cycle, respectively. Due to the decreased inhibitory inputs from the PCs, the cycle-averaged mean $f_{VN}(t)$ increases monotonically from 44.3 Hz, and it becomes saturated at 71.5 Hz at about the 300th cycle. Also, the modulation of $f_{VN}(t)$ increases from 20.2 Hz, and it gets saturated at 32.5 Hz at about the 300th cycle. As a result of effective inhibitory coordination of PCs, a big modulation occurs in M_{VN} .

The learning gain degree \mathcal{L}_g , corresponding to the modulation gain ratio, is given by the normalized modulation of $f_{VN}(t)$ divided by that at the 1st cycle:

$$\mathcal{L}_g = \frac{M_{VN}}{M_{VN} \text{ at the 1st cycle}}, \quad (33)$$

where M_{VN} at the 1st cycle is 20.2 Hz. Figure 11(d) shows a plot of \mathcal{L}_g versus cycle. \mathcal{L}_g increases monotonically from 1, and it becomes saturated at about the 300th cycle. Thus, we get the saturated learning gain degree \mathcal{L}_g^* ($\simeq 1.608$). As will be seen in the next subsection, \mathcal{L}_g^* ($\simeq 1.608$) is the largest one among the available ones. Hence, in the optimal case of $p_c^* = 0.06$ where spiking patterns of GR clusters with the diversity degree D^* ($\simeq 1.613$) are the most diverse, motor learning for the OKR adaptation with the saturated learning gain degree \mathcal{L}_g^* ($\simeq 1.608$) is the most effective.

Learning progress may be seen clearly in the IO system. During the learning cycle, the IO neuron receives both the excitatory desired signal for a desired eye-movement and the inhibitory signal from the VN neuron (denoting a realized eye-movement). We introduce the learning progress degree \mathcal{L}_p , given by the ratio of the time-averaged inhibitory input from the VN neuron to the time-averaged excitatory input of the desired signal:

$$\mathcal{L}_p = \frac{\bar{I}_{\text{GABA}}^{(\text{IO}, \text{VN})}}{|\bar{I}_{\text{AMPA}}^{(\text{IO}, \text{DS})}|}, \quad (34)$$

where $\bar{I}_{\text{GABA}}^{(\text{IO}, \text{VN})}$ is the cycle-averaged inhibitory GABA receptor-mediated current from the VN to the IO, and

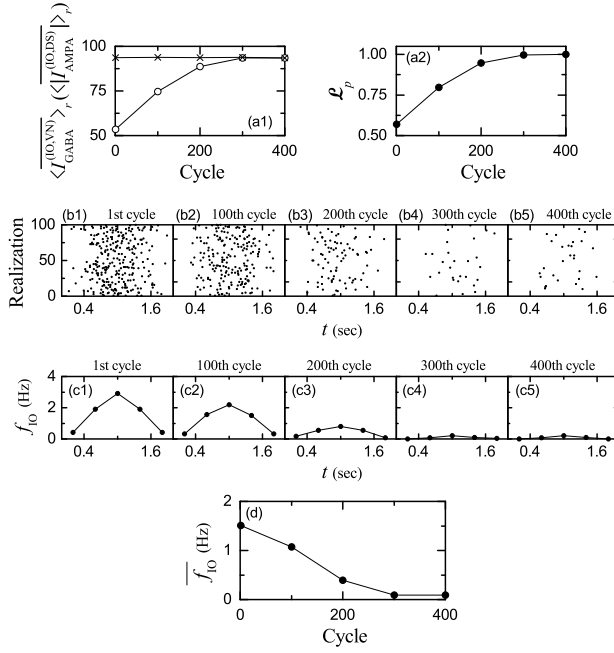


FIG. 12: Change in firing activity of the IO neuron during learning in the optimal case of $p_c^* = 0.06$. Plots of (a1) realization-average for the time-averaged inhibitory synaptic current from the VN neuron ($\langle I_{\text{GABA}}^{(\text{IO}, \text{VN})} \rangle_r$) (open circles) and realization-average for the time-averaged excitatory synaptic current from the IO desired signal ($\langle |I_{\text{AMPA}}^{(\text{IO}, \text{DS})}| \rangle_r$) versus cycle; number of realizations (\dots_r) is 100. (a2) Plot of learning progress degree \mathcal{L}_p versus cycle. (b1)-(b5) Raster plots of spikes of the IO neuron (i.e., collection of spike trains for all the realizations; number of realizations is 100) and (c1)-(c5) bin-averaged instantaneous individual firing rate $f_{\text{IO}}(t)$; the bin size is $\Delta t = 400$ msec. (d) Plot of cycle-averaged individual firing rate $f_{\text{IO}}(t)$ versus cycle.

$I_{\text{AMPA}}^{(\text{IO}, \text{DS})}$ is the cycle-averaged excitatory AMPA receptor-mediated current into the IO via the desired signal; no (excitatory) NMDA receptors exist on the IO.

Figure 12(a1) shows plots of $I_{\text{GABA}}^{(\text{IO}, \text{VN})}$ (open circles) and $I_{\text{AMPA}}^{(\text{IO}, \text{DS})}$ (crosses) versus cycle in the optimal case of $p_c^* = 0.06$. With increasing the cycle, the cycle-averaged inhibitory input from the VN neuron increases, and converges to the constant cycle-averaged excitatory input through the IO desired signal. Thus, as shown in Fig. 12(a2), \mathcal{L}_p increases with cycle, and at about the 300th cycle, it becomes saturated at $\mathcal{L}_p = 1$. In this saturated case, the cycle-averaged excitatory and inhibitory inputs to the IO are balanced.

We also study the firing activity of IO during learning process. Figures 12(b1)-12(b5) and Figures 12(c1)-12(c5) show cycle-evolutions of raster plots of spikes of the IO neuron (i.e., collection of spike trains for all the realizations; number of realizations is 100) and the bin-averaged instantaneous individual firing rates f_{IO} (i.e., the number of spikes of the IO neuron in a bin with the bin width

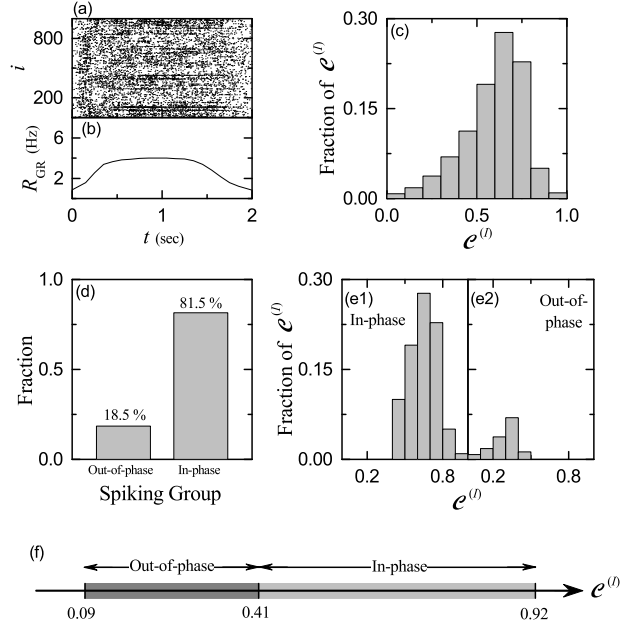


FIG. 13: Highly-connected case of $p_c = 0.6$. (a) Raster plot of spikes of 10^3 randomly chosen GR cells. (b) Instantaneous whole-population spike rate $R_{\text{GR}}(t)$ in the whole population of GR cells. Band width for $R_{\text{GR}}(t)$: $h = 10$ msec. (c) Distribution of conjunction indices $\{C^{(I)}\}$ for the GR clusters in the whole population. (d) Fraction of spiking groups. Distributions of $\{C^{(I)}\}$ for the (e1) in-phase and (e2) out-of-phase spiking groups. Bin size for the histograms in (c) and (e1)-(e2) is 0.1. (f) Ranges of $\{C^{(I)}\}$ in the in-phase and the out-of-phase spiking groups.

$\Delta t = 100$ msec), respectively. In the 1st cycle, relatively dense spikes appear at the middle stage of the cycle in the raster plot of spikes, due to the effect of excitatory IO desired signal. However, with increasing the cycle, spikes at the middle stage become sparse, because of increased inhibitory input from the VN neuron. In this case, the bin-averaged instantaneous individual firing rate $f_{\text{IO}}(t)$ of the IO neuron forms a bell-shaped curve due to the sinusoidally-modulating desired input into the IO. With increasing the cycle, the amplitude of $f_{\text{IO}}(t)$ decreases due to the inhibitory input from VN, and it becomes saturated at about the 300th cycle. Thus, the cycle-averaged individual firing rate $f_{\text{IO}}(t)$ is decreased from 1.51 Hz to 0.09 Hz, as shown in Fig. 12(d). The firing output of the IO neuron is fed into the PCs via the CFs. Hence, with increasing the cycle, the error-teaching CF instructor signals become weaker and saturated at about the 300th cycle.

While the saturated CF signals are fed into the PCs, saturation for the cycle-averaged bin-averaged synaptic weights $\langle \tilde{J}(t) \rangle$ appears [see Fig. 7(c)]. Then, the subsequent learning process in the PC-VN system also becomes saturated, and we get the saturated learning gain degree $\mathcal{L}_g^*(\simeq 1.608)$, which is shown in Fig. 11(d).

E. Dependence of Diversity Degree \mathcal{D} and Learning Gain Degree \mathcal{L}_g on p_c (Connection Probability from GO to GR Cells)

In the above subsections, we consider only the optimal case of $p_c^* = 0.06$ (i.e., 6%) where the spiking patterns of the GR clusters are the most diverse. From now on, we vary the connection probability p_c from GO to GR cells, and investigate the dependence of the diversity degree \mathcal{D} for the spiking patterns of the GR clusters and the learning gain degree \mathcal{L}_g on p_c .

We first consider the highly-connected case of $p_c = 0.6$ (i.e., 60%). Figure 13(a) shows the raster plot of spikes of 10^3 randomly chosen GR cells, and the population-averaged firing activity in the whole population of GR cells may be well seen in the instantaneous whole-population spike rate $R_{\text{GR}}(t)$ in Fig. 13(b). As shown in Fig. 2(b), each GR cluster is bounded by two glomeruli (corresponding to the terminals of the MFs) at both ends. Each glomerulus receives inhibitory inputs from nearby 81 GO cells with the connection probability $p_c = 0.6$. Hence, on average, about 49 GO cell axons innervate each glomerulus. Then, each GR cell in a GR cluster receives about 97 inhibitory inputs via two dendrites which contact the two glomeruli at both ends. Due to the increased inhibitory inputs from the pre-synaptic GO cells, spike density in the raster plot is decreased, and the top part of $R_{\text{GR}}(t)$ becomes lowered and broadly flattened, in comparison with the optimal case in Fig. 4(b). Thus, $R_{\text{GR}}(t)$ becomes more different from the firing rate f_{MF} for the MF signal in Fig. 1(b1).

GR cells in each GR cluster shares the same inhibitory and the excitatory inputs through their dendrites which synaptically contact the two glomeruli at both ends. Thus, GR cells in each GR cluster exhibit similar firing activity. Then, similar to the case of $R_{\text{GR}}(t)$, the cluster-averaged firing activity in the I th GR cluster ($I = 1, \dots, 2^{10}$) may be well described in terms of its instantaneous cluster spike rate $R_{\text{GR}}^{(I)}(t)$ of Eq. (23). In this case, the conjunction index $\mathcal{C}^{(I)}$ of the I th GR cluster (representing the similarity degree between the spiking behavior $[R_{\text{GR}}^{(I)}(t)]$ of the I th GR cluster and that of the whole population $[R_{\text{GR}}(t)]$) is given by the cross-correlation at the zero time lag between $R_{\text{GR}}^{(I)}(t)$ and $R_{\text{GR}}(t)$ [see Eq. (24)].

Figure 13(c) shows the distribution of conjunction indices $\{\mathcal{C}^{(I)}\}$ with a peak at 0.65. When compared with the optimal case in Fig. 6(a) with a peak at 0.55, the whole distribution is moved to the right, and the values of $\{\mathcal{C}^{(I)}\}$ for all the GR clusters are positive. Thus, all the anti-phase and complex out-of-phase spiking patterns with negative values of $\{\mathcal{C}^{(I)}\}$ disappear. Only the in- and out-of-phase spiking patterns with positive values of $\{\mathcal{C}^{(I)}\}$ persist. Consequently, the mean of the distribution $\{\mathcal{C}^{(I)}\}$ is increased to 0.613, while the standard deviation is decreased to 0.125, in comparison to the optimal case where the mean and the standard deviation are

0.320 and 0.516, respectively. Then, the diversity degree \mathcal{D} of the spiking patterns $[R_{\text{GR}}^{(I)}(t)]$ of all the GR clusters, representing a quantitative measure for diverse recoding in the granular layer, is given by the relative standard deviation for the distribution $\{\mathcal{C}^{(I)}\}$ [see Eq. (25)]. In the highly-connected case of $p_c = 0.6$, its diversity degree is $\mathcal{D} \simeq 0.204$ which is much smaller than \mathcal{D}^* ($\simeq 1.613$) in the optimal case.

The reduction in \mathcal{D} for the spiking patterns (corresponding to the firing outputs) of the GR clusters arises due to decrease in differences between the total synaptic inputs into each GR clusters. As the connection probability p_c from the GO to GR cells is increased, differences between the total inhibitory synaptic inputs from the pre-synaptic GO cells into each GR clusters are decreased due to increase in the number of pre-synaptic GO cells. On the other hand, the excitatory inputs into each GR clusters via MFs are Poisson spike trains with the same firing rates, and hence they are essentially the same. Thus, differences between the total synaptic inputs (including both the inhibitory and the excitatory inputs) into each GR clusters become reduced. These less different inputs into the GR clusters produce less different outputs (i.e. spiking patterns) of the GR clusters, which leads to decreases in the diversity degree \mathcal{D} in the highly-connected case.

We decompose the whole GR clusters into the in- and the out-of-phase spiking groups. Unlike the optimal case of $p_c^* = 0.06$, no anti-phase spiking group appears. Figure 13(d) shows the fraction of spiking groups. The in-phase spiking group is a major one with fraction 81.5%, while the out-of-phase spiking group is a minor one with fraction 18.5%. In comparison with the optimal case where the fraction of in-phase spiking group is 50.2%, the fraction of in-phase spiking group for $p_c = 0.6$ is so much increased. In this highly-connected case, the spiking-group ratio, given by the ratio of the fraction of the in-phase spiking group to that of the out-of-phase spiking group, is $\mathcal{R} \simeq 4.405$ which is much larger than that ($\mathcal{R}^* \simeq 1.008$) in the optimal case. Thus, good balance between the in- and the out-of-phase spiking groups in the optimal case becomes broken up because the in-phase spiking group is a dominant one. In this unbalanced case, the diversity degree \mathcal{D} for the spiking patterns of GR clusters is decreased so much.

Figures 13(e1) and 13(e2) also show plots of conjunction indices $\mathcal{C}^{(I)}$ of the GR clusters in the in- and out-of-phase spiking groups, respectively. The ranges for the distributions of $\mathcal{C}^{(I)}$ in the two spiking groups are also given in the bar diagram in Fig. 13(f). In the case of in-phase spiking group, the distribution of $\mathcal{C}^{(I)}$ with a peak at 0.65 has positive values in the range of (0.41, 0.92). When compared with the optimal case where the range is (0.39, 0.85), the range in the highly-connected case of $p_c = 0.6$ is shifted to the right and a little widened. Also, the mean and standard deviation for $p_c = 0.6$ are 0.677 and 0.094, respectively. In comparison with the optimal case where the mean is 0.538 and the standard deviation

is 0.181, the relative standard deviation for $p_c = 0.6$ is much reduced.

Also, in the case of the out-of-phase spiking group, the distribution of $\mathcal{C}^{(I)}$ with a peak at 0.35 has only positive values in the range of (0.09, 0.41), and its mean and standard deviations are 0.325 and 0.067, respectively. Unlike the optimal case, there are no out-of-phase spiking patterns with negative values of $\mathcal{C}^{(I)}$. Only out-of-phase spiking patterns which are developed from the in-phase spiking patterns appear, and hence they have just positive values of $\mathcal{C}^{(I)}$. Thus, the range for $p_c = 0.6$ is moved to the positive region, and it becomes narrowed, in comparison to the optimal case where the range is (-0.20, 0.39). Also, the relative standard deviation for $p_c = 0.6$ is much decreased, in comparison to the optimal case where the mean and the standard deviation are 0.102 and 0.328, respectively.

In the optimal case of $p_c^* = 0.06$, the in- and the out-of-phase spiking groups are shown to play their own roles for synaptic plasticity at the PF-PC synapses, respectively. As a result of cooperation in their good-balanced state, effective depression (strong/weak LTD) at the PF-PC synapses occurs, which eventually leads to effective motor learning for OKR adaptation in the PC-VN-IO system. On the other hand, in the highly-connected case of $p_c = 0.6$, the in-phase spiking group becomes a dominant one, and hence good balance between the in- and the out-of-phase spiking groups is broken up. In such an unbalanced state, contribution of the out-of-phase spiking group to the synaptic plasticity at the PF-PC synapses is decreased so much, which is clearly shown below.

Figure 14 shows change in synaptic weights of active PF-PC synapses and firing activity of PCs during learning in the highly-connected case of $p_c = 0.6$. Cycle-evolution of bin-averaged synaptic weights $\langle \tilde{J}(t) \rangle$ (solid circles) of active PF signals is shown in Figs. 14(a1)-14(a5). For comparison, data for $\langle \tilde{J}(t) \rangle$ (open circles) in the optimal case of $p_c^* = 0.06$ are also given. In comparison with the optimal case, the bin-averaged synaptic weights $\langle \tilde{J}(t) \rangle$ at the middle stage are less depressed, while at the initial and the final stages, they are more depressed. Thus, the modulation of $\langle \tilde{J}(t) \rangle$ is reduced so much. This small modulation is distinctly in contrast to the big modulation in the optimal case. $\langle \tilde{J}(t) \rangle$ also becomes saturated at about the 300th cycle, as in the optimal case.

The degree of depression changes depending on the relative phase difference between the PF (student) signals and the error-teaching (instructor) CF signals. The CF signals are in-phase ones with respect to the firing rate $f_{DS}(t)$ of the Poisson spike trains for the IO desired signal for a desired eye-movement in Fig. 1(b2), and the PF signals are classified as in- and out-of-phase signals with respect to the instantaneous whole-population spike rate $R_{GR}(t)$. We note that, depending on p_c the reference signal $R_{GR}(t)$ has a varying “similarity” degree relative to the sinusoidally-modulating IO desired signal $f_{DS}(t)$. With increasing p_c , the top part of $R_{GR}(t)$ becomes more

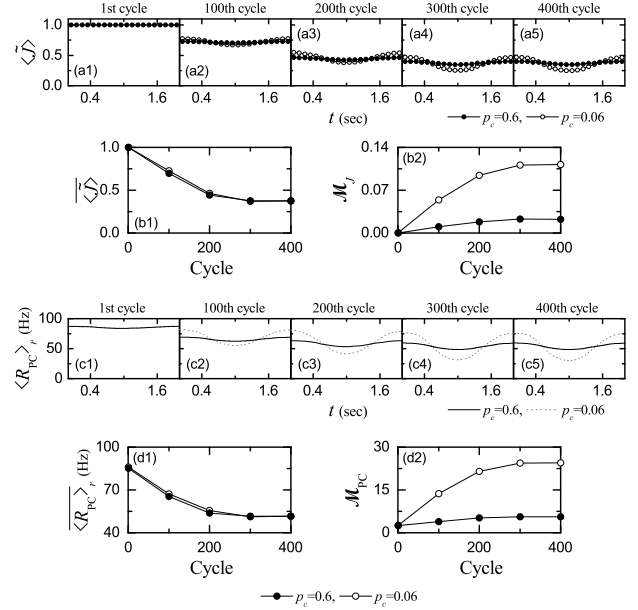


FIG. 14: Change in synaptic weights of active PF-PC synapses and firing activity of PCs during learning in the highly-connected case of $p_c = 0.6$; for comparison, data in the optimal case of $p_c^* = 0.06$ are also given. (a1)-(a5) Cycle-evolution of bin-averaged (normalized) synaptic weights $\langle \tilde{J}(t) \rangle$ of active PF signals (bin size: $\Delta t = 100$ msec). Plots of (b1) cycle-averaged mean $\langle \tilde{J}(t) \rangle$ and (b2) modulation \mathcal{M}_J for $\langle \tilde{J}(t) \rangle$ versus cycle. (c1)-(c5) Realization-averaged instantaneous population spike rate $\langle R_{PC}(t) \rangle_r$; the number of realizations is 100. Plots of (d1) cycle-averaged mean $\langle R_{PC}(t) \rangle_r$ and (d2) modulations \mathcal{M}_{PC} for $\langle R_{PC}(t) \rangle_r$ versus cycle. In (a1)-(a5), (b1)-(b2), and (d1)-(d2), solid (open) circles represent data in the case of $p_c = 0.6$ (0.06). In (c1)-(c5), solid (dotted) lines denote data in the case of $p_c = 0.6$ (0.06).

broadly flattened, and hence its similarity with respect to $f_{DS}(t)$ is decreased; the similarity degree may be quantitatively measured in terms of the cross-correlation at the zero-time lag between $R_{GR}(t)$ and $f_{DS}(t)$. Hence, due to decrease in the similarity degree between $R_{GR}(t)$ and $f_{DS}(t)$, on average, in-phase PF signals for $p_c = 0.6$ are less depressed by the CF signals than those in the optimal case. Thus, in the highly-connected case of $p_c = 0.6$, the bin-averaged synaptic weights $\langle \tilde{J}(t) \rangle$ at the middle stage are less depressed than those in the optimal case.

In the optimal case, at the initial and the final stages, weak LTD occurs at the PF-PC synapses, in contrast to strong LTD at the middle stage. This kind of weak LTD arises due to the major contribution of the out-of-phase spiking group with a larger fraction at the initial and the final stages, while strong LTD takes place at the middle stage due to the dominant contribution of the in-phase spiking group. However, in the highly-connected case of $p_c = 0.6$, the fraction of the out-of-phase spiking group is so much reduced. Hence, the contribution of the in-phase spiking group becomes larger even at the initial and the final stages. Thus, the bin-averaged synaptic

weights $\langle \tilde{J}(t) \rangle$ at the initial and the final stages are more depressed than those in the optimal case.

Figures 14(b1) and 14(b2) show plots of cycle-averaged mean $\langle \tilde{J}(t) \rangle$ and modulation \mathcal{M}_J for $\langle \tilde{J}(t) \rangle$ versus cycle, respectively; $p_c = 0.6$ (solid circles) and $p_c^* = 0.06$ (open circles). Both the cycle-averaged mean $\langle \tilde{J}(t) \rangle$ and the modulation \mathcal{M}_J for $\langle \tilde{J}(t) \rangle$ become saturated at about the 300th cycle. With increasing the cycle, the cycle-averaged mean $\langle \tilde{J}(t) \rangle$ decreases from 1 to 0.374 due to LTD at the PF-PC synapses, similar to the optimal case of $p_c^* = 0.06$ where $\langle \tilde{J}(t) \rangle$ decreases from 1 to 0.372. On the other hand, the modulation \mathcal{M}_J increases very slowly from 0 to 0.023, in contrast to the optimal case with a big modulation where it increases quickly from 0 to 0.112. When compared with the optimal case, bin-averaged synaptic weights $\langle \tilde{J}(t) \rangle$ at the initial and the final stages come down more rapidly (i.e., they are more depressed), while at the middle stage, they come down relatively slowly (i.e., they are less depressed). This kind of less effective synaptic plasticity at the PF-PC synapses arises due to the dominant fraction of the in-phase spiking group (i.e., the in-phase spiking group makes a major contribution at the initial and the final stages as well as at the middle stage). As a result, the modulation \mathcal{M}_J makes a slow increase to its saturated value ($= 0.023$), which is markedly in contrast to the optimal case with a big modulation.

We next consider the effect of PF-PC synaptic plasticity with a reduced small modulation on the subsequent learning process in the PC-VN system. Figures 14(c1)-14(c5) show cycle-evolution of realization-averaged instantaneous population spike rate $\langle R_{PC}(t) \rangle_r$ (number of realizations: 100); $p_c = 0.6$ (solid line) and $p_c^* = 0.06$ (dotted line). As a result of PF-PC synaptic plasticity, $\langle R_{PC}(t) \rangle_r$ becomes lower at the middle stage than at the initial and the final stages. Thus, $\langle R_{PC}(t) \rangle_r$ forms a well-shaped curve, and it becomes saturated at about the 300th cycle. However, due to the ineffective PF-PC synaptic plasticity, the modulation of $\langle R_{PC}(t) \rangle_r$ for $p_c = 0.6$ becomes so small, in contrast to the optimal case with a big modulation (which arises from the effective PF-PC synaptic plasticity).

Figures 14(d1) and 14(d2) show plots of cycle-averaged mean $\langle R_{PC}(t) \rangle_r$ and modulation \mathcal{M}_{PC} for $\langle R_{PC}(t) \rangle_r$ versus cycle, respectively; $p_c = 0.6$ (solid circles) and $p_c^* = 0.06$ (open circles). Both $\langle R_{PC}(t) \rangle_r$ and \mathcal{M}_{PC} become saturated at about the 300th cycle. With increasing the cycle, the cycle-averaged mean $\langle R_{PC}(t) \rangle_r$ decreases from 86.1 Hz to 51.8 Hz due to LTD at the PF-PC synapses, similar to the optimal case where $\langle R_{PC}(t) \rangle_r$ decreases from 86.1 Hz to 51.7 Hz. On the other hand, the modulations \mathcal{M}_{PC} increases slowly from 2.6 Hz to 5.6 Hz, which is distinctly in contrast to the optimal case where it increases rapidly from 2.6 Hz to 24.1 Hz. Thus, a small modulation occurs in \mathcal{M}_{PC} due to the ineffective depression at the PF-PC synapses under an unbalanced state between the in- and the out-of-phase spiking

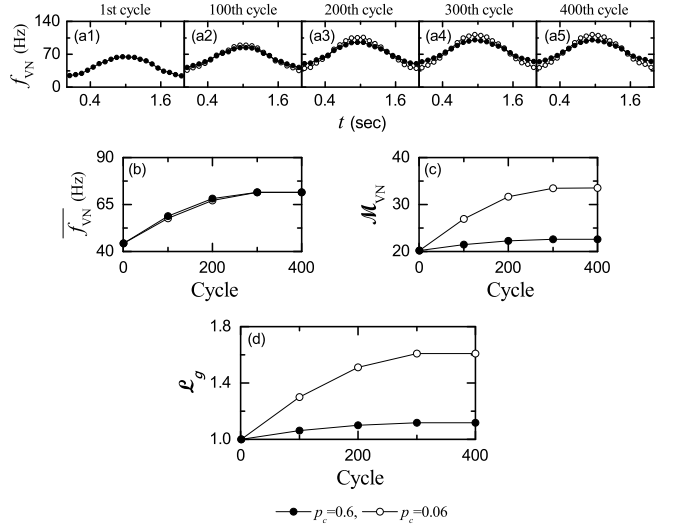


FIG. 15: Change in firing activity of the VN neuron during learning in the highly-connected case of $p_c = 0.6$; for comparison, data in the optimal case of $p_c^* = 0.06$ are also given. (a1)-(a5) Bin-averaged instantaneous individual firing rates $f_{VN}(t)$; the bin size is $\Delta t = 100$ msec. Plots of (b) cycle-averaged mean $f_{VN}(t)$ and (c) modulation \mathcal{M}_{VN} for $f_{VN}(t)$, and (d) learning gain degree \mathcal{L}_g versus cycle. In (a1)-(a5) and (b)-(d), solid (open) circles represent data for $p_c = 0.6$ (0.06).

groups. These principal PCs of the cerebellar cortex also exert ineffective inhibitory coordination on the VN neuron which evokes OKR eye-movement.

Change in firing activity of the VN neuron during learning in the highly-connected case of $p_c = 0.6$ (solid circles) is shown in Fig. 15; for comparison, data in the optimal case of $p_c^* = 0.06$ (open circles) are also given. Figures 15(a1)-15(a5) show cycle-evolution of bin-averaged instantaneous individual firing rate $f_{VN}(t)$. It seems to be saturated at about the 300th cycle. Due to the inhibitory coordination of PCs on the VN neuron, the maximum of $f_{VN}(t)$ occurs at the middle stage, while the minimum appears at the initial and the final stages. Thus, $f_{VN}(t)$ forms a bell-shaped curve, in contrast to the well-shaped curves of $\langle R_{PC}(t) \rangle_r$. However, due to the ineffective inhibitory coordination of the PCs, the modulation of $f_{VN}(t)$ becomes smaller than that in the optimal case.

Figures 15(b) and 15(c) show plots of cycle-averaged mean $f_{VN}(t)$ and modulation \mathcal{M}_{VN} for $f_{VN}(t)$. Both $f_{VN}(t)$ and \mathcal{M}_{VN} become saturated at about the 300th cycle. $f_{VN}(t)$ increases from 44.3 Hz to 71.4 Hz, which is nearly the same as that in the optimal case where it increases from 44.3 Hz to 71.5 Hz. \mathcal{M}_{VN} also increases slowly from 20.2 Hz to 22.6 Hz, which is in contrast to the optimal case where \mathcal{M}_{VN} increases quickly from 20.2 Hz to 32.5 Hz. Then, the learning gain degree \mathcal{L}_g , given by the normalized gain ratio, is shown in Fig. 15(d). \mathcal{L}_g increases from 1 and becomes saturated at $\mathcal{L}_g^* \simeq 1.118$ at

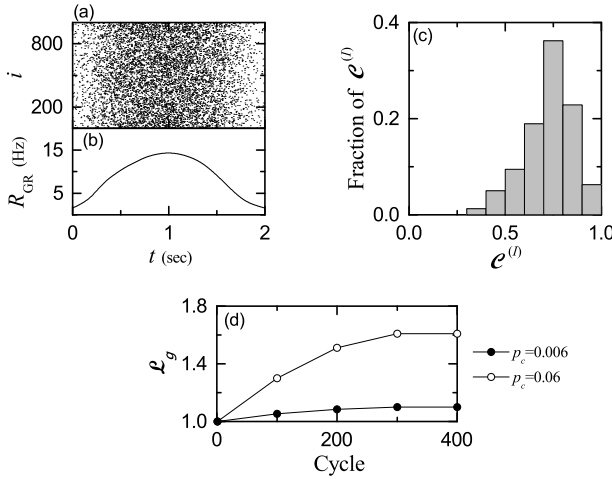


FIG. 16: Lowly-connected case of $p_c = 0.006$. (a) Raster plot of spikes of 10^3 randomly chosen GR cells. (b) Instantaneous whole-population spike rate $R_{GR}(t)$ in the whole population of GR cells. Band width for $R_{GR}(t)$: $h = 10$ msec. (c) Distribution of conjunction indices $\{C^{(I)}\}$ for the GR clusters in the whole population. (d) Plot of learning gain degree \mathcal{L}_g (solid circles) versus cycle; for comparison, data (open circles) in the optimal case of $p_c^* = 0.06$ are also given.

about the 300th cycle which is smaller than the saturated learning gain degree \mathcal{L}_g^* ($\simeq 1.608$) in the optimal case. Consequently, due to the ineffective coordination of PCs, the saturated learning gain degree becomes smaller.

To sum up the highly-connected case of $p_c = 0.6$, good balance between the in- and the out-of-phase spiking group in the optimal case ($\mathcal{R}^* \simeq 1.008$) is broken up, because the fraction of in-phase spiking group becomes dominant ($\mathcal{R} \simeq 4.405$). Thus, the diversity degree for the spiking patterns of the GR clusters is so much decreased ($\mathcal{D} \simeq 0.204$), in comparison with \mathcal{D}^* ($\simeq 1.613$) in the optimal case. Due to the unbalance between the in- and the out-of-phase spiking group, synaptic plasticity at the PF-PC synapses becomes ineffective, which also results in ineffective motor learning for the OKR eye-movement.

We next consider the lowly-connected cases of $p_c = 0.006$ (i.e. 0.6 %). Figure 16(a) and 16(b) show the raster plot of randomly-chosen 10^3 GR cells and the instantaneous whole-population spike rate $R_{GR}(t)$ in the whole population of GR cells for $p_c = 0.006$, respectively. In this lowly-connected case, the inhibitory inputs from GO cells into the GR clusters is so much reduced, and the excitatory MF signals into the GR clusters become dominant inputs. Hence, the raster plot becomes more dense, and $R_{GR}(t)$ becomes more similar to the firing rate $f_{MF}(t)$ of the Poisson spike train for the MF signal in Fig. 1(b1), in contrast to the highly-connected case of $p_c = 0.6$ with broadly flattened top part in $R_{GR}(t)$ [see Fig. 13(b)].

Due to so much decrease in inhibitory inputs from the GO cells into the GR clusters, only the in-phase spiking group [where spiking patterns are similar to $f_{MF}(t)$]

appears (i.e., all the out-of-phase spiking group disappears), which is distinctly in contrast to the optimal case of $p_c^* = 0.06$ where diverse spiking groups such as the in-, anti-, and complex out-of-phase spiking groups exist. The distribution of conjunction indices $\{C^{(I)}\}$ of the GR clusters ($\mathcal{C}^{(I)}$): representing the similarity degree between the spiking behavior [$R_{GR}^{(I)}(t)$: instantaneous cluster spike rate] of the I th GR cluster and that [$R_{GR}(t)$] in the whole population) is shown in Fig. 16(c). In comparison to the optimal case in Fig. 6(a), the distribution is shifted to the positive region, due to existence of only the in-phase GR clusters with positive values of $C^{(I)}$. Thus, it has a peak at 0.75, and its range is (0.32, 0.98).

In this lowly-connected case, the mean and the standard deviation for the distribution of $\{C^{(I)}\}$ are 0.737 and 0.129, respectively, which is in contrast to the optimal case with the smaller mean (= 0.320) and the larger standard deviation (= 0.516). Then, the diversity degree \mathcal{D} of the spiking patterns of all the GR clusters, given by the relative standard deviation for the distribution $\{C^{(I)}\}$ [see Eq. (25)], is $\mathcal{D} \simeq 0.175$ which is much smaller than \mathcal{D}^* ($\simeq 1.613$) in the optimal case. Consequently, the degree in diverse recoding in the granular layer is so much reduced in the lowly-connected case of $p_c = 0.006$, due to the existence of only the in-phase spiking group without the out-of-phase spiking group.

We also compare the lowly-connected case of $p_c = 0.006$ with the highly-connected case of $p_c = 0.6$ in Fig. 13. The diversity degree \mathcal{D} ($\simeq 0.204$) for $p_c = 0.6$ is also much reduced in comparison with \mathcal{D}^* ($\simeq 1.613$) in the optimal case. However, it is a little larger than $\mathcal{D} \simeq 0.175$ for $p_c = 0.006$, because for $p_c = 0.6$ a minor out-of-phase spiking group with positive values of $C^{(I)}$ exists, along with the major in-phase spiking group. We also note that, the in-phase spiking patterns in both the lowly- and the highly-connected cases have completely different waveforms. For $p_c = 0.006$ the in-phase spiking patterns are more similar to the sinusoidally-modulating MF signal $f_{MF}(t)$, while those for $p_c = 0.6$ are more different from $f_{MF}(t)$ due to broad flatness in their top part. In this way, there are two independent ways via increase or decrease in p_c from the optimal value p_c^* (= 0.06) to break up the good balance between the in- and the out-of-phase spiking groups, which results in decrease in the diversity degree in recoding of the GR cells.

Due to the reduced diversity in recoding of the GR cells, the modulation for the bin-averaged synaptic weights $\langle \tilde{J}(t) \rangle$ is much decreased, in contrast to the big modulation in the optimal case of $p_c^* = 0.06$. This ineffective synaptic plasticity at the PF-PC synapses leads to reduced modulation in the realization-averaged instantaneous population spike rate $\langle R_{PC}(t) \rangle_r$ of the principal PCs in the cerebellar cortex which also exert ineffective inhibitory coordination on the VN neuron which produces the final output of the cerebellum. Then, the modulation in the bin-averaged instantaneous individual firing rate $f_{VN}(t)$ of the VN neuron is much decreased. Plots of the learning gain degree \mathcal{L}_g [corresponding to the

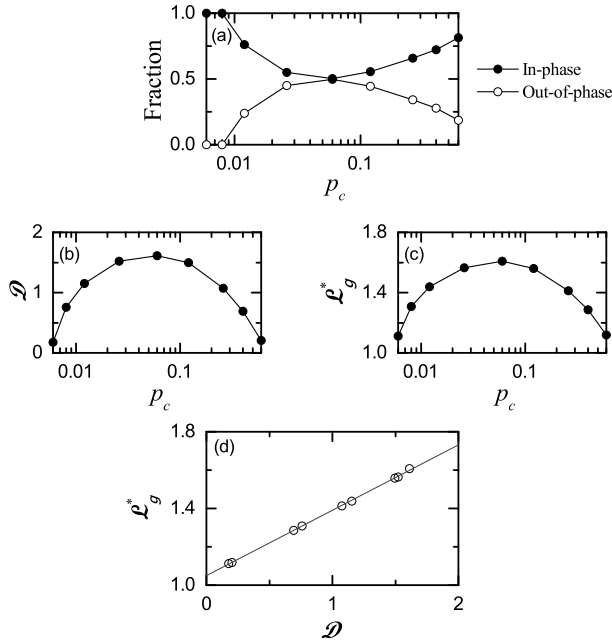


FIG. 17: Strong correlation between the diversity degree \mathcal{D} and the saturated learning gain degree \mathcal{L}_g^* . (a) Fraction of in- (solid circles) and out-of-phase (open circles) spiking groups. (b) Plot of diversity degree \mathcal{D} for the spiking patterns of all the GR clusters versus p_c . (c) Saturated learning gain degree \mathcal{L}_g^* versus p_c . (d) Plot of \mathcal{L}_g^* versus \mathcal{D} .

modulation gain ratio for $f_{VN}(t)$] are shown in Fig. 16(d) in both the lowly-connected case of $p_c = 0.006$ (solid circles) and the optimal case of $p_c^* = 0.06$ (open circles). For $p_c = 0.006$ \mathcal{L}_g increases very slowly and becomes saturated at $\mathcal{L}_g^* \simeq 1.099$ at about the 300th cycle. This saturated learning gain degree $\mathcal{L}_g^* \simeq 1.099$ is much smaller than that ($\mathcal{L}_g^* \simeq 1.608$) in the optimal case. Consequently, low diversity in recoding of the GR cells for $p_c = 0.006$ results in ineffective motor learning for the OKR adaptation.

Finally, based on the above two examples for the highly- and the lowly-connected cases, we investigate dependence of the diversity degree \mathcal{D} for the spiking patterns of the GR clusters and the saturated learning gain degree \mathcal{L}_g^* on p_c by varying it from the optimal value ($p_c^* = 0.06$). Figure 17(a) shows plots of fractions of the in- and the out-of-phase spiking groups versus p_c . The fraction of the in-phase spiking group (solid circles) forms a well-shaped curve with a minimum at $p_c = p_c^* (= 0.06)$, while the fraction of the out-of-phase spiking group (open circles) forms a bell-shaped curve with a maximum at the optimal value of $p_c^* = 0.06$. For sufficiently small p_c , we have two sample cases where the fraction of in-phase spiking group is 1 (i.e., the fraction of out-of-phase spiking group is 0). We note that, in the optimal case of $p_c^* = 0.06$, fractions of the in- (50.2%) and the out-of-phase spiking (49.8%) groups are well balanced (i.e., good balance between the in- and the out-of-phase spik-

ing groups). As p_c is changed (i.e., increased or decreased) from p_c^* , the fraction of the in-phase spiking group increases, and then the spiking-group ratio \mathcal{R} (i.e., the ratio of the fraction of the in-phase spiking group to that of the out-of-phase spiking group) increases from the golden spiking-group ratio \mathcal{R}^* ($\simeq 1.008$) in the optimal case.

Figures 17(b) and 17(c) show plots of the diversity degree \mathcal{D} for the spiking patterns of the GR clusters and the saturated learning gain degree \mathcal{L}_g^* versus p_c , respectively. The diversity degrees \mathcal{D} forms a bell-shaped curve with a maximum \mathcal{D}^* ($\simeq 1.613$) in the optimal case of $p_c^* = 0.06$ with the golden spiking-group ratio $\mathcal{R}^* \simeq 1.008$ (i.e., good balance between the in- and the out-of-phase spiking group). We note that, in this optimal case where the recoding of the GR cells is the most diverse, the saturated learning gain degree \mathcal{L}_g^* also has its maximum ($\mathcal{L}_g^* \simeq 1.608$). As p_c is changed (i.e., increased or decreased) from the optimal value ($= 0.06$), the spiking-group ratio \mathcal{R} is increased, because of increase in the fraction of in-phase spiking group. Then, the diversity degree \mathcal{D} in recodings of the GR cells becomes decreased, which also results in decrease in the saturated learning gain degree \mathcal{L}_g^* from the maximum. Thus, \mathcal{L}_g^* also forms a bell-shaped curve, as in the case of \mathcal{D} , and they have their maxima at the optimal values ($p_c^* = 0.06$).

Figure 17(d) shows a plot of \mathcal{L}_g^* versus \mathcal{D} . As shown clearly in Fig. 17(d), both \mathcal{L}_g^* and \mathcal{D} have a strong correlation with the Pearson's correlation coefficient $r \simeq 0.9998$. Consequently, the more diverse in recoding of the GR cells, the more effective in motor learning for the OKR adaptation.

IV. SUMMARY AND DISCUSSION

We are interested in the gain adaptation of OKR for the eye movement. Diverse experimental works on the OKR have been done in rabbits, mice, and zebrafishes [24–31]. Moreover, some features of OKR adaptation were successfully reproduced through computational simulations in the adaptive filter model [34] and the spiking network model [20]. However, effects of diverse recording of GR cells on the OKR adaptation in previous computational works are necessary to be more clarified in several dynamical aspects. Particularly, the previous works lacked complete dynamical classification of diverse spiking patterns of GR cells and their association with the error-teaching CF signals. We note that such dynamical classification of diverse recording of GR cells may be a basis for clear understanding synaptic plasticity at PF-PC synapses and the subsequent learning progress in the PC-VN-IO system.

In contrast to the previous works, we first made a complete dynamical classification of spiking patterns of GR clusters in a cerebellar ring network. We mainly considered an optimal case of p_c^* ($= 0.06$) where the spiking patterns of GR clusters are the most diverse. Collec-

tive firing activity in the whole population of GR cells (receiving excitatory inputs from MFs) may be well described in terms of its instantaneous whole-population spike rate $R_{\text{GR}}(t)$. Although it is in-phase with the MF signal, $R_{\text{GR}}(t)$ has a central flattened plateau due to the inhibitory inputs from GO cells. This whole population of GR cells is divided into 2^{10} GR clusters. GR cells in each I th GR cluster ($I = 1, \dots, 2^{10}$) show similar spiking behaviors, and their averaged firing activity is described by the instantaneous cluster spike rate $R_{\text{GR}}^{(I)}(t)$ in the I th GR cluster. Then, GR clusters have been found to exhibit diverse spiking patterns for $R_{\text{GR}}^{(I)}(t)$ which are in-, anti-, and complex out-of-phase with respect to the instantaneous whole-population spike rate $R_{\text{GR}}(t)$.

The diverse spiking patterns are grouped into the in-phase and the out-of-phase (including both anti- and complex out-of-phase spiking patterns) spiking groups. The fraction of in-phase (out-of-phase) spiking group is 50.2 (49.8)%, and hence the spiking-group ratio (given by the ratio of the fraction of in-phase spiking group to that of the out-of-phase spiking group) is $\mathcal{R}^* \simeq 1.008$. In this case, the spiking pattern of each I th GR cluster has been quantitatively characterized in terms of its conjunction index $\mathcal{C}^{(I)}$, given by the cross-correlation at the zero-time lag between the instantaneous cluster spike rate $R_{\text{GR}}^{(I)}(t)$ and the instantaneous whole-population spike rate $R_{\text{GR}}(t)$, representing the degree for the conjunction of the spiking behavior of each I th GR cluster with that of the whole population [i.e., denoting the degree for the resemblance between $R_{\text{GR}}^{(I)}(t)$ and $R_{\text{GR}}(t)$]. The distribution for $\{\mathcal{C}^{(I)}\}$ forms a bell-shaped curve. Then, the diversity of spiking patterns of all GR clusters is quantitatively characterized in terms of the diversity degree \mathcal{D} , given by the relative standard deviation (i.e. the standard deviation divided by the mean) of the distribution $\{\mathcal{C}^{(I)}\}$. In the optimal case of $p_c^* = 0.06$, $\mathcal{D}^* \simeq 1.613$, which is a quantitative measure for the diversity of spiking patterns of all GR clusters in the granular layer.

Next, based on the dynamical classification of diverse spiking patterns of GR clusters in the optimal case of $p_c^* = 0.06$, we made an intensive investigation on their effects on synaptic plasticity at PF-PC synapses and the subsequent learning process in the PC-VN-IO system. At all stages in the whole learning process, in-phase and out-of-phase spiking groups have been found to play their own roles, respectively. Both the diversely-recoded PF (student) signals from GR cells and the error-teaching CF (instructor) signals from the IO are fed into the PCs. We note that the CF signals are also in-phase with respect to the instantaneous whole-population spike rate $R_{\text{GR}}(t)$ in the whole population of GR cells.

In-phase PF signals have been found to be strongly depressed (i.e., strong LTD) by the in-phase CF signals, while out-of-phase PF signals have been found to be weakly depressed (i.e., weak LTD) by the in-phase CF signals due to the phase difference between the PF and the CF signals. At the middle stage of a learning cycle,

fraction of in-phase PF spikes is dominant (i.e., fraction of out-of-phase PF spikes may be negligible). On the other hand, at the initial and the final stages, the fraction of out-of-phase PF spikes is comparable to that of in-phase PF spikes. Hence, the bin-averaged synaptic weights of active PF signals have been found to form a well-shaped curve (i.e., appearance of a minimum at the middle stage and maxima at both the initial and final stages). In this way, at the PF-PC synapses, diversely-recoded PF student signals are effectively depressed by the error-teaching CF instructor signals.

Due to this kind of effective depression at PF-PC synapses, the (realization-averaged) instantaneous population spike rate $\langle R_{\text{PC}}(t) \rangle_r$ of PCs (corresponding to the principal outputs of the cerebellar cortex) has also been found to form a well-shaped curve with a minimum at the middle stage. Consequently, a big modulation occurs in $\langle R_{\text{PC}}(t) \rangle_r$. These PCs exert effective inhibitory coordination on the VN neuron (which evokes OKR eye-movement). Thus, the (realization-averaged) instantaneous individual firing rate f_{VN} of the VN neuron has been found to form a bell-shaped curve with a maximum at the middle stage. In this case, the learning gain degree \mathcal{L}_g , corresponding to the modulation gain ratio (i.e., normalized modulation divided by that at the 1st cycle for f_{VN}), has been found to increase with learning cycle and to be saturated at about the 300th cycle. The saturated learning gain degree in the optimal case of $p_c^* = 0.06$ was $\mathcal{L}_g^* (\simeq 1.608)$.

During the learning cycle, the inhibitory input from the VN neuron (representing a realized eye-movement) is fed into the IO neuron, along with the excitatory IO desired signal for a desired eye-movement from the PCN. In this case, learning progress is characterized in terms of the learning progress degree \mathcal{L}_p , given by the ratio of the time-averaged inhibitory input from the VN neuron to the time-averaged excitatory input of the IO desired signal. As the learning cycle is increased, the time-averaged inhibitory input increases, and converges to the constant time-averaged excitatory input. Thus, with increasing the learning cycle, the learning progress degree \mathcal{L}_p has been found to increase and eventually become saturated at $\mathcal{L}_p = 1$ at about the 300th cycle. In this saturated case, the time-averaged excitatory and inhibitory inputs to the IO neuron become balanced.

One of our main concerns is to investigate the effect of the connection probability p_c (from GO to GR cells) on diverse recoding of GR cells. By varying (i.e., increasing or decreasing) p_c from its optimal value $p_c^* (= 0.06)$, the fraction of in-phase spiking group has been found to increase. Thus, the spiking-group ratio \mathcal{R} (i.e., the ratio of the fraction of in-phase spiking group to that of the out-of-phase spiking group) has the golden ratio $\mathcal{R}^* (\simeq 1.008)$ as its minimum value for $p_c^* = 0.06$. Thus, in the optimal case of $p_c^* = 0.06$, the fractions between the in- and the out-of-phase spiking groups are well balanced (i.e., good balance between the in- and the out-of-phase spiking groups), which leads to the most diversity in spiking

patterns of GR clusters. Also, in this optimal case, each GR cell receives inhibitory inputs from about 10 nearby GO cells. In [20, 36] where the parameter values were taken, based on physiological data, the average number of nearby GO cell axons innervating each GR cell is about 8, which is close to that in the optimal case. Hence, we hypothesize that the granular layer in the cerebellar cortex has evolved toward the goal of the most diverse recording.

As the spiking-group ratio \mathcal{R} is increased from the golden ratio \mathcal{R}^* , the diversity degree \mathcal{D} for the spiking patterns of all the GR clusters decreases due to increase in the fraction of in-phase spiking group. Thus, the curve of \mathcal{D} has been found to form a bell-shaped curve with a maximum $\mathcal{D}^*(\simeq 1.613)$ at $p_c = p_c^*$. Accordingly, in the optimal case ($p_c^* = 0.06$), spiking patterns of the GR clusters are the most diverse. In this case, a plot of saturated learning gain degree \mathcal{L}_g^* versus p_c has also been found to form a bell-shaped curve with a peak $\mathcal{L}_g^*(\simeq 1.608)$ at $p_c = p_c^*$. Thus, both the saturated learning gain degree \mathcal{L}_g^* and the diversity degree \mathcal{D} have a strong correlation with the Pearson's correlation coefficient $r \simeq 0.9998$. Consequently, the more diverse in recoding of GR cells, the more effective in the OKR adaptation for the eye movement.

Finally, we discuss limitations of our present work and future works. In the present work, we did not take into consideration intra-population synaptic connections, and hence no motor rhythms appear in the presence of just inter-population synaptic connections. When we add intra-population couplings between inhibitory GO cells, a granular motor rhythm of $7 \sim 25$ Hz may appear in the granular layer (i.e., GR-GO feedback system) [70]. Ultrafast motor rhythm of ~ 200 Hz may also appear in the Purkinje (molecular) layer by adding intra-population synaptic connections between PCs (BCs) [71]. In the system of IO neurons, ~ 10 Hz motor rhythm appears in the presence of electric gap junctions between IO neurons [72]. Hence, in a future work, it would be interesting to investigate the effect of motor rhythms on diverse recoding of GR cells and learning process in the PC-VN-IO system by adding intra-population couplings. Beyond the synaptic plasticity at PF-PC synapses (considered in this work), diverse synaptic plasticity occurs at other synapses in the cerebellum [73] such as synaptic plasticity at PF-BC and BC-PC [74], at MF-cerebellar nucleus and PC-cerebellar nucleus [75], and at MF-GR cells [76]. Therefore, as a future work, it would be interesting to study the effect of diverse synaptic plasticity at other synapses on cerebellar motor learning. In addition to variation in p_c , another possibility to change synaptic inputs into the GR cells is to vary NMDA receptor-mediated maximum conductances $\bar{g}_{\text{NMDA}}^{(\text{GR})}$ and $\bar{g}_{\text{NMDA}}^{(\text{GO})}$, associated with persistent long-lasting firing activities. It would also be interesting to investigate the effect of NMDA receptor-mediated synaptic inputs on diverse recoding of GR cells and motor learning in the OKR adaptation by changing $\bar{g}_{\text{NMDA}}^{(\text{GR})}$ and $\bar{g}_{\text{NMDA}}^{(\text{GO})}$. This work is

TABLE I: Parameter values for LIF neuron models with AHP currents for the granule (GR) cell and the Golgi (GO) cell in the granular layer, the Purkinje cell (PC) and the basket cell (BC) in the Purkinje-molecular layer, and the vestibular nucleus (VN) and the inferior olive (IO) neurons; units of the capacitance, the conductance, the potential, the current, and the time are pF, nS, mV, pA, and msec, respectively.

X-population	Granular Layer		Purkinje -Molecular Layer		VN neuron	IO neuron
	GR cell	GO cell	PC	BC		
C_X	3.1	28.0	107.0	107.0	122.3	10.0
$I_L^{(X)}$	$g_L^{(X)}$	0.43	2.3	2.32	2.32	1.63
	$V_L^{(X)}$	-58.0	-55.0	-68.0	-68.0	-56.0
$I_{AHP}^{(X)}$	$\bar{g}_{AHP}^{(X)}$	1.0	20.0	100.0	100.0	50.0
	$\tau_{AHP}^{(X)}$	5.0	5.0	5.0	2.5	2.5
	$V_{AHP}^{(X)}$	-82.0	-72.7	-70.0	-70.0	-70.0
	$v_{th}^{(X)}$	-35.0	-52.0	-55.0	-55.0	-38.8
$I_{ext}^{(X)}$	0.0	0.0	250.0	0.0	700.0	0.0

beyond the scope of the present work, and hence it is left as a future work.

Acknowledgments

This research was supported by the Basic Science Research Program through the National Research Foundation of Korea (NRF) funded by the Ministry of Education (Grant No. 20162007688).

Appendix: Parameter Values for The LIF Neuron Models and The Synaptic Currents

In this appendix, we list four tables which show parameter values for the LIF neuron models in Subsec. II C and the synaptic currents in Subsec. II D. These values are adopted from physiological data [20, 36].

For the LIF neuron models, the parameter values for the capacitance C_X , the leakage current $I_L^{(X)}$, the AHP current $I_{AHP}^{(X)}$, and the external constant current $I_{ext}^{(X)}$ are shown in Table I.

For the synaptic currents, the parameter values for the maximum conductance $\bar{g}_R^{(T)}$, the synaptic weight $J_{ij}^{(T,S)}$, the synaptic reversal potential $V_R^{(S)}$, the synaptic decay time constant $\tau_R^{(T)}$, and the amplitudes A_1 and A_2 for the type-2 exponential-decay function in the granular layer, the Purkinje-molecular layer, and the other parts for the VN and IO are shown in Table II.

TABLE II: Parameter values for synaptic currents $I_R^{(T,S)}(t)$ into the granule (GR) and the Golgi (GO) cells in the granular layer, the Purkinje cells (PCs) and the basket cells (BCs) in the Purkinje-molecular layer, and the vestibular nucleus (VN) and the inferior olive (IO) neurons in the other parts. In the granular layer, the GR cells receive excitatory inputs via mossy fibers (MFs) and inhibitory inputs from GO cells, and the GO cells receive excitatory inputs via parallel fibers (PFs) from GR cells. In the Purkinje-molecular layer, the PCs receive two types of excitatory inputs via parallel fibers (PFs) from GR cells and through climbing fibers (CFs) from the IO and one type of inhibitory inputs from the BCs. The BCs receive excitatory inputs via PFs from GR cells. In the other parts, the VN neuron receives excitatory inputs via MFs and inhibitory inputs from PCs, and the IO neuron receives excitatory input via one desired signal (DS) and inhibitory input from the VN neuron.

Target Cells (T)	Granular Layer				Purkinje-Molecular Layer				VN neuron			IO neuron		
	GR		GO		PC			BC	VN		IO			
Source Cells (S)	MF	MF	GO	PF	PF	PF	CF	BC	PF	MF	MF	PC	DS	VN
Receptor (R)	AMPA	NMDA	GABA	AMPA	NMDA	AMPA	AMPA	GABA	AMPA	AMPA	NMDA	GABA	AMPA	GABA
$\bar{g}_R^{(T)}$	0.18	0.025	0.028	45.5	30.0	0.7	0.7	1.0	0.7	50.0	25.8	30.0	1.0	0.18
$J_{ij}^{(T,S)}$	8.0	8.0	10.0	0.00004	0.00004	0.006	1.0	5.3	0.006	0.002	0.002	0.008	1.0	5.0
$V_R^{(S)}$	0.0	0.0	-82.0	0.0	0.0	0.0	0.0	-75.0	0.0	0.0	0.0	-88.0	0.0	-75.0
$\tau_R^{(T)}$	1.2	52.0	7.0, 59.0	1.5	31.0, 170.0	8.3	8.3	10.0	8.3	9.9	30.6	42.3	10.0	10.0
A_1, A_2			0.43, 0.57		0.33, 0.67									

-
- [1] M. Ito, *The Cerebellum and Neural Control* (Raven Press, New York, 1984).
- [2] M. Ito, Ann. N. Y. Acad. Sci. **978**, 273 (2002).
- [3] M. Ito, *The Cerebellum: Brain for an Implicit Self* (Pearson Education Inc., New Jersey, 2012).
- [4] S. Gilman, J. Bloedel, and R. Lechtenberg, *Disorders of the Cerebellum* (F.A. Davis Company, Philadelphia, 1981).
- [5] M. U. Manto, *Cerebellar Disorders; A Practical Approach to Diagnosis and Managements* (Cambridge University Press, Cambridge, 2010).
- [6] D. Marr, J. Physiol. **202**, 437 (1969).
- [7] J. S. Albus, Math. Biosci. **10**, 25 (1971).
- [8] D. O. Hebb, *The Organization of Behavior; A Neuropsychological Theory* (Wiley & Sons, New York, 1949).
- [9] G. S. Brindley, IBRO Bull. **3**, 80 (1964).
- [10] P. Strata, J. Physiol. **587**, 5519 (2009).
- [11] T. Tyrrell and D. Willshaw, Phil. Trans. R. Soc. Lond. B **336**, 239 (1992).
- [12] P. Safo and W. G. Regehr, Neuropharmacology **54**, 213 (2008).
- [13] M. Ito, Brain Res. **886**, 237 (2000).
- [14] M. Ito, M. Sakurai, and P. Tongroach, J. Physiol. **324**, 113 (1982).
- [15] M. Ito and M. Kano, Neurosci. Lett. **33**, 253 (1982).
- [16] M. Sakurai, J. Physiol. **394**, 463 (1987).
- [17] M. Ito, Ann. Rev. Neurosci. **12**, 85 (1989).
- [18] M. Ito, Physiol. Rev. **81**, 1143 (2001).
- [19] M. Ito, Nat. Rev. Neurosci. **3**, 896 (2002).
- [20] T. Yamazaki and S. Nagao, PLoS One **7**, e33319 (2012).
- [21] M. Ito, Trends Cogn. Sci. **2**, 313 (1998).
- [22] M. D. Mauk and N. H. Donegan, Learn. Mem. **3**, 130 (1997).
- [23] K. M. Christian and R. F. Thompson, Learn. Mem. **11**, 427 (2003).
- [24] S. Nagao, Exp. Brain Res. **53**, 36 (1983).
- [25] S. Nagao, Exp. Brain Res. **73**, 489 (1988).
- [26] R. J. Harvey, C. De'Sperati, and P. Strata, Vision Res. **37**, 1615 (1997).
- [27] M. Iwashita, R. Kanai, K. Funabiki, K. Matsuda, and T. Hirano, Neurosci. Res. **39**, 299 (2001).
- [28] Y.-Y. Huang and S. C. F. Neuhauss, Front. Biosci. **13**, 1899 (2008).
- [29] H. Tabata, N. Shimizu, Y. Wada, K. Miura, and K. Kawano, J. Vis. **10**, 13 (2010).
- [30] H. Matsuno, M. Kudoh, A. Watakabe, T. Yamamori, R. Shigemoto, and S. Nagao, PLoS ONE **11**, e0164037 (2016).
- [31] S. D. Scheetz, E. Shao, Y. Zhou, C. L. Cario, Q. Bai, and E. A. Burton, J. Neurosci. Meth. **293**, 329 (2017).
- [32] H. Gomi and M. Kawato, Biol. Cybern. **68**, 105 (1992).
- [33] M. Fujita, Biol. Cybern. **45**, 195 (1982).
- [34] P. Dean, J. Porrill, C.-F. Ekerot, and H. Jörntell, Nat. Rev. Neurosci. **11**, 30 (2010).
- [35] T. J. Sejnowski, J. Math. Biol. **4**, 303 (1977).
- [36] T. Yamazaki and S. Tanaka, Eur. J. Neurosci. **26**, 2279 (2007).
- [37] S.-Y. Kim and W. Lim, J. Neurosci. Meth. **226**, 161 (2014).
- [38] X.-J. Wang, Physiol. Rev. **90**, 1195 (2010).
- [39] N. Brunel, J. Comput. Neurosci. **8**, 183 (2000).
- [40] N. Brunel and V. Hakim, Neural Comput. **11**, 1621 (1999).
- [41] N. Brunel and X.-J. Wang, J. Neurophysiol. **90**, 415 (2003).
- [42] C. Geisler, N. Brunel, and X.-J. Wang, J. Neurophysiol. **94**, 4344 (2005).
- [43] N. Brunel and D. Hansel, Neural Comput. **18**, 1066

- (2006).
- [44] N. Brunel and V. Hakim, *Chaos* **18**, 015113 (2008).
- [45] K. Pearson, *Proc. Royal Soc. Lond.* **58**, 240 (1895).
- [46] A. Mathy, S. S. N. Ho, J. T. Davie, I. C. Duguid, B. A. Clark, and M. Häusser, *Neuron* **62**, 388 (2009).
- [47] R. R. Llinás, *Front. Neural Circuit.* **7**, 96 (2014).
- [48] W. Gerstner and W. Kistler, *Spiking Neuron Models* (Cambridge University Press, New York, 2002).
- [49] W. T. Thach, *J. Neurophysiol.* **31**, 785 (1968).
- [50] M. Häusser and B. A. Clark, *Neuron* **19**, 665 (1997).
- [51] E. De Schutter, *Trends Neurosci.* **18**, 291 (1995).
- [52] C. Chen and R. F. Thompson, *Learn. Mem.* **2**, 185 (1995).
- [53] S.-H. Wang, W. Denk, and M. Häusser, *Nat. Neurosci.* **3**, 1266 (2000).
- [54] M. Coesmans, J. T. Weber, C. I. De Zeeuw, and C. Hansel, *Neuron* **44**, 691 (2004).
- [55] V. Steuber, W. Mittmann, F. E. Hoebeek, R. A. Silver, C. I. De Zeeuw, M. Häusser, and E. De Schutter, *Neuron* **54**, 121 (2007).
- [56] V. Lev-Ram, S. B. Mehta, D. Kleinfeld, and R. Y. Tsien, *Proc. Natl. Acad. Sci. USA* **100**, 15989 (2003).
- [57] E. Molnár, *J. Neurochem.* **131**, 1 (2014).
- [58] Y. Yang and S. G. Lisberger, *Nature* **510**, 529 (2014).
- [59] A. R. Gallimore, T. Kim, K. Tanaka-Yamamoto, and E. De Schutter, *Cell Rep.* **22**, 722 (2018).
- [60] W. Gerstner and J. L. van Hemmen, *Network* **3**, 139 (1992).
- [61] D. V. Buonomano and M. D. Mauk, *Neural Comput.* **6**, 38 (1994).
- [62] G. T. Kenyon, J. F. Medina, and M. D. Mauk, *J. Comput. Neurosci.* **5**, 17 (1998).
- [63] J. F. Medina, K. S. Garcia, W. L. Nores, N. M. Taylor, and M. D. Mauk, *J. Neurosci.* **20**, 5516 (2000).
- [64] P. D. Roberts, *J. Comput. Neurosci.* **22**, 283 (2007).
- [65] P. Achard and E. De Schutter, *Front. Comput. Neurosci.* **2**, 8 (2008).
- [66] G. Bouvier, J. Aljadeff, C. Clopath, C. Bimbard, J. Ranft, A. Blot, J.-P. Nadal, N. Brunel, V. Hakim, and B. Barbour, *eLife* **7**, e31599 (2018).
- [67] T. Yamazaki and S. Tanaka, *Neural Netw.* **20**, 290 (2007).
- [68] W. Maass, T. Natschläger, and H. Markram, *Neural Comput.* **14**, 2531 (2002).
- [69] H. Shimazaki and S. Shinomoto, *J. Comput. Neurosci.* **29**, 171 (2010).
- [70] E. D'Angelo, S. K. E. Koekkoek, P. Lombardo, S. Solinas, E. Ros, J. Garrido, M. Schonewille, and C. I. De Zeeuw, *Neuroscience* **162**, 805 (2009).
- [71] C. de Solages, G. Szapiro, N. Brunel, V. Hakim, P. Isope, P. Buisseret, C. Rousseau, B. Barbour, and C. Léna, *Neuron* **58**, 775 (2008).
- [72] R. R. Llinás, *J. Physiol.* **589**, 3423 (2011).
- [73] C. Hansel, D. J. Linden, and E. D'Angelo, *Nat. Neurosci.* **4**, 467 (2001).
- [74] W. Lennon, T. Yamazaki, and R. Hecht-Nielsen, *Front. Comput. Neurosci.* **9**, 150 (2015).
- [75] N. Zheng and I. M. Raman, *Cerebellum* **9**, 56 (2010).
- [76] E. D'Angelo and C. I. De Zeeuw, *Trends Neurosci.* **32**, 30 (2008).